

---

# Generating Directed Graphs with Dual Attention and Asymmetric Encoding

---

Alba Carballo-Castro\*, Manuel Madeira, Yiming Qin, Dorina Thanou, Pascal Frossard  
LTS4, EPFL, Lausanne, Switzerland

## Abstract

Directed graphs naturally model systems with asymmetric, ordered relationships, essential to applications in biology, transportation, social networks, and visual understanding. Generating such graphs enables tasks such as simulation, data augmentation and novel instance discovery; however, directed graph generation remains underexplored. We identify two key factors limiting progress in this direction: first, modeling edge directionality introduces a substantially larger dependency space, making the underlying distribution harder to learn; second, the absence of standardized benchmarks hinders rigorous evaluation. Addressing the former requires more expressive models that are sensitive to directional topologies. We propose DIRECTO, the first generative model for directed graphs built upon the discrete flow matching framework. Our approach combines: (i) principled positional encodings tailored to asymmetric pairwise relations, (ii) a dual-attention mechanism capturing both incoming and outgoing dependencies, and (iii) a robust, discrete generative framework. To support evaluation, we introduce a benchmark suite covering synthetic and real-world datasets. It shows that our method performs strongly across diverse settings and even competes with specialized models for particular classes, such as directed acyclic graphs. Our results highlight the effectiveness and generality of our approach, establishing a solid foundation for future research in directed graph generation.

## 1 Introduction

Directed graphs (digraphs) naturally model systems with asymmetric relationships, capturing essential structures such as flows, dependencies, and hierarchies that arise in many real-world applications. This makes digraphs particularly well-suited for problems in diverse domains including biology [37, 64, 71], transportation [12], social dynamics [58], and, more recently, image and video understanding [10, 57], where structured, directional representations are critical for interpretation and reasoning. Consequently, generating digraphs is central to tasks such as simulation, data augmentation and novel instance discovery in domains characterized by directional structure.

Graph generative models offer a data-driven approach to producing plausible and diverse samples, with applications in drug discovery [47, 68], finance [40], social network modeling [65], and medicine [50]. Despite their broad applicability and strong performance, the vast majority of existing generative models focus on undirected graphs [41, 46, 67, 60, 74, 17, 55]. Digraphs have received comparatively less attention, with recent work proposing auto-regressive models for DAGs [77, 39] and, more recently, for general digraphs [36]. We identify two main factors behind this limited progress. First, at the modeling level, the directed setting is inherently more challenging than its undirected counterpart, as edge directionality greatly enlarges the learnable space (see Fig. 1a: for graphs with 4 nodes, there are 218 possible digraphs, compared to only 11 undirected ones). This is further amplified in settings where domain-specific structural constraints must be respected, such as *directed acyclic graphs* (DAGs). Second, beyond these technical challenges, we identify the lack of

---

\*Correspondence to [alba.carballocastro@epfl.ch](mailto:alba.carballocastro@epfl.ch)

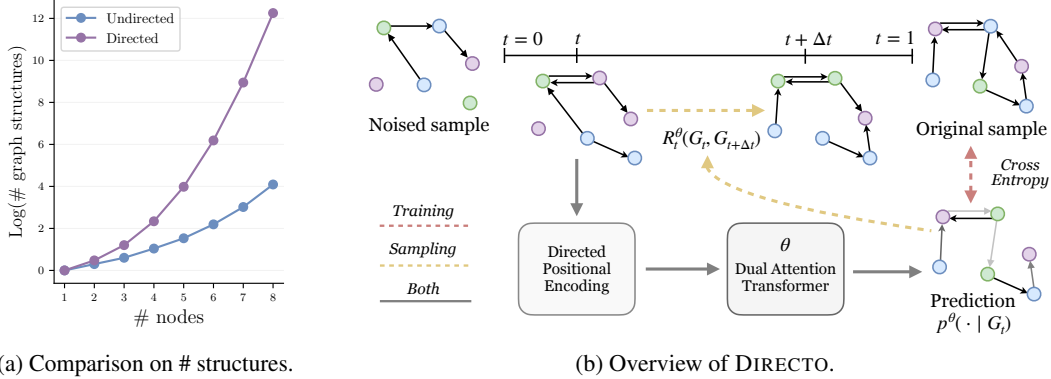


Figure 1: (a) The learnable space increases drastically with the number of nodes for digraphs compared to undirected graphs [23], highlighting challenges in extending graph generative models to directed structures. (b) Overview of our generative model for directed graphs. During training, the *dual attention transformer* (denoising network) parameterized by  $\theta$ , and enhanced with *asymmetric positional encodings*, learns to reverse predictions using cross-entropy loss. During inference, we compute the *rate matrix*  $R_t^\theta(G_t, G_{t+\Delta t})$  based on the model prediction  $p^\theta(\cdot | G_t)$ , which governs the evolution of the generative process over finite intervals  $\Delta t$ .

standardized benchmarks for directed graph generation as an important barrier to rigorous evaluation and fair comparison across methods. Current methods[39] typically rely on proxy metrics derived from downstream task performance, without directly evaluating generated graph quality.

To address the first challenge, we introduce DIRECTO<sup>2</sup>, the first iterative refinement-based generative model for directed graphs. Our approach brings together three core components of expressive graph generative modeling: (i) informative input features, (ii) an expressive neural architecture, and (iii) a robust generative framework. For input features, we find that, upon comprehensive evaluation, positional encodings specifically designed for graphs with an asymmetric adjacency matrix, are more successful than directionality-agnostic baselines. For the architecture, we employ a dual attention mechanism that performs cross-attention between edge features and their reversed counterparts, capturing both source-to-target and target-to-source information flow. Finally, these components are integrated within a robust discrete-state flow matching framework that enables efficient generation with state-of-the-art performance. Figure 1b gives an overview of our method and its components.

To tackle the second challenge, we propose a benchmarking framework for rigorous evaluation of directed graph generation. It spans both synthetic and real-world datasets and systematic evaluation metrics tailored to directed graphs. The synthetic benchmarks cover different distributions, including acyclic and community-based graphs, while real-world benchmarks include a DAG-focused dataset for *Neural Architecture Search* (NAS) [54] and a scene understanding dataset [35]. We evaluate DIRECTO on the proposed benchmarks, where it consistently achieves strong performance across all settings, underscoring its effectiveness across structurally diverse datasets. Extensive ablations further reveal that the proposed dual attention mechanism is critical for modeling directional dependencies, while positional encodings enhance overall generation quality.

Our main contributions are summarized as follows:

- (i) We propose DIRECTO, the first flow-based generative model specifically tailored for directed graphs, combining a direction-aware dual attention block with positional encoding tailored to capture directionally asymmetric structural properties.
- (ii) We address the lack of benchmarks for directed graph generation by releasing a unified evaluation pipeline that encompasses both synthetic graphs with important structural properties and real-world datasets with meaningful applications.
- (iii) We conduct an extensive empirical analysis demonstrating that DIRECTO achieves state-of-the-art performance on structurally diverse synthetic and real-world graphs.

Overall, by addressing the two main bottlenecks in directed graph generation, we aim to lay the groundwork for future research and practical deployment of directed graph generation.

<sup>2</sup>Code available at: <https://github.com/acarballocastro/DIRECTO>

## 2 Background: Discrete Flow Matching for Graph Generation

**Notation** We denote by  $G = (x^{(1:n:N)}, e^{(1:i \neq j:N)})$  directed graphs with  $N$  nodes. The set of nodes is denoted by  $\{x^{(n)}\}_{n=1}^N$ , and the set of directed edges by  $\{e^{(i,j)}\}_{1 \leq i \neq j \leq N}$ . Both nodes and edges are categorical variables, where  $x^{(n)} \in \{1, \dots, X\}$  and  $e^{(i,j)} \in \{1, \dots, E\}$ .

**Problem statement** Graph generative models aim to learn the underlying probability distribution over graphs that produced a given dataset, enabling the generation of new samples that preserve the structural patterns and properties of the training graphs. Recently, *Discrete Flow Matching* (DFM)-based models [20, 9] have achieved state-of-the-art performance in undirected graph generation [55]. DFM belongs to a broader class of discrete state-space methods that recover the original graph distribution  $\mathbf{p}_1$  by progressively denoising samples from a pre-specified noise distribution  $\mathbf{p}_{\text{noise}}$  [67, 74, 60]. By operating directly in the discrete spaces, these methods naturally align with the discreteness of graphs and are well-suited to capturing complex dependencies through iterative refinement. DFM distinguishes itself from other methods in this class by decoupling sampling from training, allowing for post-training sampling optimization. This additional layer of expressivity is particularly valuable for digraphs, where edge directionality introduces combinatorial complexity and exponentially expands the search space. We now introduce the two main processes of DFM: the *noising* and *denoising* processes.

**Noising process** We use a subscript  $t$  to denote variables at time  $t$ , e.g.,  $x_t^{(n)}$  or  $e_t^{(i,j)}$ . The noising process then runs from  $t = 1$  to  $t = 0$ , progressively corrupting the original input graphs through a linear interpolation between the data distribution and the limit distribution  $\mathbf{p}_0 = \mathbf{p}_{\text{noise}}$ . This interpolation is applied independently to each variable [20, 9], corresponding to each node and edge in the case of graphs. For example, for each node  $x_1^{(n)}$ , its noisy distribution at step  $t$  is defined as:

$$p_{t|1}^X(x_t^{(n)} | x_1^{(n)}) = t \delta(x_t^{(n)}, x_1^{(n)}) + (1-t) p_{\text{noise}}^X(x_t^{(n)}), \quad (1)$$

where  $\delta(\cdot, \cdot)$  denotes the Kronecker delta and  $p_{\text{noise}}^X$  is the limit distribution over node categories. A similar construction is used for the edges [55].

**Denoising process** The denoising process aims to reverse the noising trajectory, running from  $t = 0$  to  $t = 1$ . It leverages a denoising neural network, parametrized by  $\theta$ , which is trained to predict the clean node  $\mathbf{p}_{1|t}^{\theta, (n)}$  and edge  $\mathbf{p}_{1|t}^{\theta, (i,j)}$  distributions given a noisy graph, aggregated as:

$$\mathbf{p}_{1|t}^\theta(\cdot | G_t) = \left( \left( \mathbf{p}_{1|t}^{\theta, (n)}(x_1^{(n)} | G_t) \right)_{1 \leq n \leq N}, \left( \mathbf{p}_{1|t}^{\theta, (i,j)}(e_1^{(i,j)} | G_t) \right)_{1 \leq i \neq j \leq N} \right). \quad (2)$$

This network is trained using a cross-entropy loss independently to each node and each edge:

$$\mathcal{L} = \mathbb{E}_{t, G_1, G_t} \left[ - \sum_n \log \left( \mathbf{p}_{1|t}^{\theta, (n)}(x_1^{(n)} | G_t) \right) - \lambda \sum_{i \neq j} \log \left( \mathbf{p}_{1|t}^{\theta, (i,j)}(e_1^{(i,j)} | G_t) \right) \right], \quad (3)$$

where the expectation is taken over time  $t$ , sampled from a predefined distribution over  $[0, 1]$  (e.g., uniform);  $G_1 \sim \mathbf{p}_1(G_1)$  is a clean graph from the dataset; and  $G_t \sim \mathbf{p}_t(G_t | G_1)$  is its noised version at time  $t$  [55]. The hyperparameter  $\lambda \in \mathbb{R}^+$  controls the relative weighting between node and edge reconstruction losses. The denoising process is then formulated as a *Continuous-Time Markov Chain* (CTMC), which starts from sampling a noisy graph  $G_0 \sim \mathbf{p}_0$  and evolves according to:

$$\mathbf{p}_{t+\Delta t|t}(G_{t+\Delta t} | G_t) = \delta(G_t, G_{t+\Delta t}) + \mathbf{R}_t(G_t, G_{t+\Delta t}) dt, \quad (4)$$

where  $\mathbf{R}_t$  is the CTMC rate matrix [9]. In practice, this update rule is approximated in two ways: first, by discretizing time with a finite step size  $\Delta t$ , in an Euler method step; and second, by approximating the ground-truth rate matrix with an estimate  $\mathbf{R}_t^\theta$  computed from the denoising network predictions  $\mathbf{p}_{1|t}^\theta(\cdot | G_t)$ . Further details are provided in Appendix I.

## 3 Generating DiGraphs with Asymmetric Encoding and Dual Attention

In this section, we introduce DIRECTO, the first flow-based digraph generative model. We begin by outlining the overall generative framework, followed by the two directionality-aware components that form the core of DIRECTO: asymmetric positional encoding and dual attention.

### 3.1 Directed Graph Generation via Discrete Flow Matching

Building on the formulation of Sec. 2, we extend DFM to the directed graph setting. Inspired by standard practice in iterative refinement for undirected graphs [67, 74, 60, 55], we assume that every ordered pair of distinct nodes corresponds to a directed edge belonging to one of several possible classes, including a class representing the absence of an edge. We provide the complete training and sampling algorithms in Appendix D.

To mitigate the combinatorial explosion induced by the asymmetric adjacency matrices in digraphs (see Figure 1a), we leverage a key advantage of DFM: its decoupling of training and sampling. This flexibility allows for post-training sampling optimization, including time-adaptive schedules and custom CTMC rate matrices [55], which we extend to the directed setting. Although these optimizations yield consistent improvements (see Appendix H.5), they alone are insufficient to fully capture the distinctive distributional and structural properties of directed graphs without incorporating additional inductive biases, as demonstrated in Section 5. To overcome this, we introduce architectural components explicitly designed to model these unique characteristics and enable effective directionality-aware graph generation.

### 3.2 Asymmetric positional encoding

The generative framework introduced above employs a denoising GNN. However, GNNs inherently struggle to capture global or higher-order patterns due to the locality of message passing [72, 48]. To maximize the capacity of our method, we augment our GNN with positional encodings (PEs) that inject structural information beyond local neighborhoods [4, 7]. Common choices for undirected graphs include Laplacian eigenvectors or shortest-path distances, which have proven effective in enriching node and edge representations for undirected graph generation [67, 55]. However, these encodings do not respect edge directionality, and thus fail to distinguish asymmetric structural roles. To overcome this limitation, we adopt recent direction-aware positional encodings [21, 27] that account for both incoming and outgoing connectivity. We append these encodings to node and edge features, allowing our model to better capture the structural dependencies unique to directed graphs.

**Magnetic Laplacian** In the undirected case, eigenvectors of the combinatorial Laplacian (Lap) rely on the spectral decomposition  $L = \Gamma \Lambda \Gamma^{-1}$  where  $L$  is the combinatorial Laplacian,  $\Lambda$  the diagonal matrix of eigenvalues, and  $\Gamma$  the matrix of eigenvectors. In the directed case, the combinatorial Laplacian can be defined as  $L_{\text{dir}} = D_s - A_s$ , where  $A_s$  is the symmetrized adjacency matrix and  $D_s$  the symmetrized degree matrix. This symmetrization discards directionality, as it enforces  $A_s = A_s^\top$ , but it is necessary to guarantee that  $L_{\text{dir}}$  is symmetric and positive semi-definite.

To retain directional information while preserving desirable spectral properties, the authors in [21] propose the *Magnetic Laplacian* (MagLap), which introduces a complex-valued phase encoding into the adjacency matrix. It is given by:

$$L_{\text{dir}}^{(q)} = D_s - (A_s \odot \exp(i\Theta^{(q)})) \tag{5}$$

where  $\odot$  denotes the element-wise (Hadamard) product,  $i$  is the imaginary unit, and the phase matrix  $\Theta^{(q)}$  is defined as  $\Theta_{u,v}^{(q)} = 2\pi q(A_{u,v} - A_{v,u})$ . The parameter  $q \geq 0$  controls the strength of the phase shift. When  $q = 0$ , the Magnetic Laplacian reduces to the classical combinatorial Laplacian. The resulting complex-valued eigenvectors can effectively encode directionality patterns in the graph, and we leverage them by concatenating the real and complex parts of the eigenvectors to the node features and the eigenvalues to the global graph features.

**Multi- $q$  Magnetic Laplacian** Recent work by [27] introduces a multi- $q$  extension of the Magnetic Laplacian, which leverages  $Q$  distinct complex-valued potentials  $q_1, \dots, q_Q$  to recover a more informative bidirectional walk profile, effectively capturing asymmetries in node connectivity. By extending the notion of the walk profile to the directed setting, this method enhances the expressiveness of the Magnetic Laplacian. In our model, we leverage this information by concatenating the first  $k$  eigenvalues (real and imaginary parts) of each of the  $Q$  magnetic Laplacians to the global features, and the corresponding first  $k$  eigenvectors to the node features, providing direction-aware structural signals to both levels of representation.

**Directed Relative Random Walk Probabilities (RRWP)** For undirected graphs, RRWP encodes the likelihood of arriving from one node to another through  $k$ -step random walks, expressed via a transition matrix  $T^k = (AD^{-1})^k$ . For digraphs, authors in [21] adapt this idea by defining  $T = AD_{out}^{-1}$ , using the degree matrix of the outgoing edges  $D_{out}^{-1}$ . To account for reverse flows, they also suggest that it is informative to additionally model reverse random walks, representing the likelihood of reaching a given edge starting from another through  $k$ -step random walks with  $R = A^\top D_{in}^{-1}$ , where  $D_{in}$  is the in-degree matrix.

Following [21], we ensure that the probabilities encoded in the matrices sum up to 1 by adding self-loops to sink nodes during pre-processing. Finally, the full positional encoding concatenates both forward and reverse walk features for the  $K$ -step transition probabilities, producing the PE:

$$\text{RRWP}(G) = [I, T, T^2, \dots, T^{K-1}, I, R, R^2, \dots, R^{K-1}] \quad (6)$$

that we concatenate to the edge features, where the diagonal elements of each matrix are used to enrich the node features. To mitigate the tendency of  $k$ -step random walks to concentrate on sink nodes for large  $k$ , we incorporate *Personalized PageRank (PPR)* features. The PPR matrix is defined in closed form as  $\text{PPR} = p_r(\mathbf{I} - (1 - p_r)\mathbf{T})^{-1}$ , where  $p_r$  denotes the restart probability.

We hypothesize that incorporating directionality-aware positional encodings improves the generative performance of digraphs. To test this, we design an ablation study that evaluates which of the described encodings provide the most informative structural signals for directed graph generation tasks. See Appendix B for a more detailed description of the positional encodings.

### 3.3 Graph transformer with dual attention

Graph Transformers [16, 56] are effective at modeling node interactions while leveraging the adjacency matrix to encode structural information. However, in directed graphs, this matrix only captures source-to-target flow, overlooking potential reverse influences that can be equally important. Generating directed graphs thus requires models that (i) capture bidirectional information flow to learn how source and target nodes influence one another, and (ii) integrate structural signals across nodes, edges, and the global graph to preserve relational dependencies and ensure coherent outputs.

To address this, our model jointly processes stacked node features  $\mathbf{X}$ , edge features  $\mathbf{E}$ , and global features  $\mathbf{y}$  through a Transformer composed of  $L$  layers of a dual attention block (see Figure 2). This dual attention mechanism introduces two key innovations: (i) an attention-based aggregation scheme that jointly captures directional information, and (ii) modulation layers to incorporate information at different levels of granularity across nodes, edges, and the global graph structure.

**Bidirectional information flow via dual attention aggregation** To model directional dependencies more effectively, we use a cross-attention mechanism between source-to-target edge features  $\mathbf{E}_{ST}$  and their reversed counterparts  $\mathbf{E}_{TS}$ , which enables the model to reason bidirectionally across edges. By explicitly attending to both directions, our architecture better captures the complex, reciprocal relationships inherent in directed graphs, improving the expressiveness and accuracy of graph generation, which builds on ideas from [69]. Concretely, we compute two directional attention maps between role-specific node projections:

$$\mathbf{Y}_{ST}[i, j] = \frac{\mathbf{Q}_S[i] \cdot \mathbf{K}_T[j]}{\sqrt{d_q}}, \quad \mathbf{Y}_{TS}[i, j] = \frac{\mathbf{Q}_T[i] \cdot \mathbf{K}_S[j]}{\sqrt{d_q}}, \quad (7)$$

where  $\mathbf{Q}_S$ ,  $\mathbf{Q}_T$ ,  $\mathbf{K}_S$ , and  $\mathbf{K}_T$  are the role-specific projections for source and target nodes, respectively, and  $d_q$  is the query feature dimension. These attention weights are modulated using edge features through a FiLM layer (see Eq. (10)), producing the updated attention maps  $\mathbf{Y}'_{ST}$  and  $\mathbf{Y}'_{TS}$ . We use  $\mathbf{Y}'_{ST}$  to update the edge features, effectively combining local edge attributes with global graph information.

To consolidate directional information, we introduce an *attention aggregation mechanism*. Instead of treating the attentions from the two directions independently, we concatenate the modulated attention maps and apply a single softmax operation to obtain unified attention weights:

$$\mathbf{A}_{\text{aggr}} = \text{softmax}(\text{concat}(\mathbf{Y}'_{ST}, \mathbf{Y}'_{TS})) \in \mathbb{R}^{n \times 2n}, \quad \mathbf{V}_{\text{aggr}}^\top = \text{concat}(\mathbf{V}_S^\top, \mathbf{V}_T^\top) \in \mathbb{R}^{2n \times h}, \quad (8)$$

where  $h$  is the hidden dimension and the concatenation operation is performed along the node dimensions. These unified weights are then used to aggregate the value vectors  $\mathbf{V}_S$  and  $\mathbf{V}_T$  through weighted summation:

$$\mathbf{X}' = \mathbf{A}_{\text{aggr}} \mathbf{V}_{\text{aggr}} \in \mathbb{R}^{n \times h}. \quad (9)$$

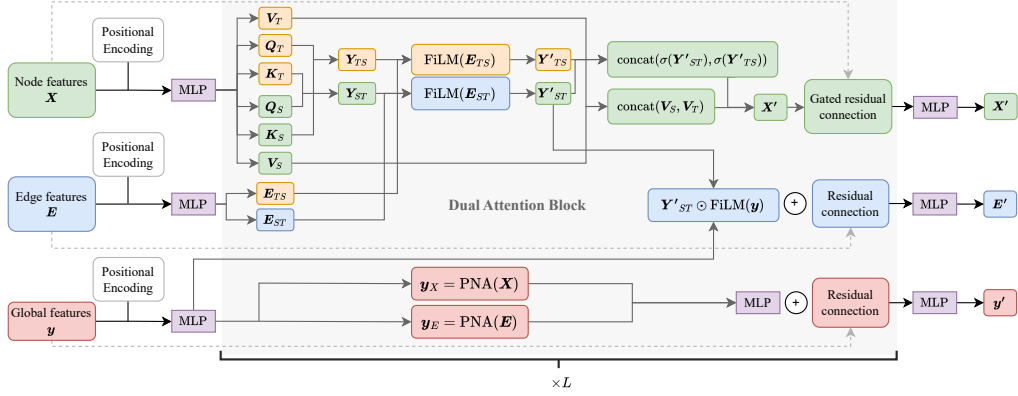


Figure 2: Network architecture of DIRECTO. We stack  $L$  dual attention layers that account for both source-to-target and target-to-source information via cross-attention mechanisms.  $\mathbf{X}$ ,  $\mathbf{E}$  and  $\mathbf{y}$  denote the stacked input node, edge, and global features.  $\mathbf{X}'$ ,  $\mathbf{E}'$  and  $\mathbf{y}'$  are the output of the model, i.e., predicted clean node and edge distribution, and graph feature. FiLM [53] and PNA [13] pooling layers are incorporated to enable flexible modulation between node, edge, and graph-level features.

This aggregation allows the model to assign asymmetric importance to the source-to-target and target-to-source directions by applying a joint softmax. The node features are then updated using a gated residual connection, which adaptively combines the original and updated features by learning a gate that controls how much of the new information should be integrated. Full technical details are provided in Appendix A

**Multi-scale information modulation for graph denoising** A graph denoising model should predict clean node and edge types from noisy inputs, which requires integrating both local interactions and global structure from node, edge, and graph-level features. Building on standard graph generation architectures [67, 60, 55], we incorporate *Feature-wise Linear Modulation* (FiLM) [53] and *Principal Neighbourhood Aggregation* (PNA) [13] layers to enhance multi-scale feature fusion.

FiLM adaptively modulates edge features using attention signals: given the edge feature matrix  $\mathbf{E}$ , the attention matrix  $\mathbf{E}_{\text{attn}}$ , and the learnable weights  $\mathbf{W}_{\text{FiLM}}^1, \mathbf{W}_{\text{FiLM}}^2$ , it computes

$$\text{FiLM}(\mathbf{E}, \mathbf{E}_{\text{attn}}) = \mathbf{E}\mathbf{W}_{\text{FiLM}}^1 + (\mathbf{E}\mathbf{W}_{\text{FiLM}}^2) \odot \mathbf{E}_{\text{attn}} + \mathbf{E}_{\text{attn}}, \quad (10)$$

where  $\odot$  denotes element-wise multiplication. These layers are also used to integrate global graph-level signals into the construction of edge representations.

To complement this, PNA layers aggregates multi-scale neighborhood information via pooling operations: given node features  $\mathbf{X} \in \mathbb{R}^{n \times h}$  and a learnable weight matrix  $\mathbf{W}_{\text{PNA}}$ , PNA computes

$$\text{PNA}(\mathbf{X}) = \text{concat}(\max(\mathbf{X}), \min(\mathbf{X}), \text{mean}(\mathbf{X}), \text{std}(\mathbf{X})) \mathbf{W}_{\text{PNA}} \in \mathbb{R}^{4h}, \quad (11)$$

with concatenation performed along the feature dimension. We use PNA layers to update global graph representations based on node-level information at each attention pass.

Together, these components enable expressive and scalable integration of local and global features, allowing the model to capture higher-order structure for accurate graph denoising.

## 4 Benchmarking Directed Graph Generation

Despite growing interest in directed graphs [63], benchmarking remains underdeveloped [5]. In particular, existing approaches to benchmarking digraph generation typically rely on performance in downstream tasks, failing to directly evaluate generative performance. With the objective of establishing standard datasets and metrics, we propose here a comprehensive benchmark that covers synthetic and real-world digraphs, along with tailored metrics for the digraph setting that directly assess key generative qualities, including sample validity, diversity, and distributional alignment.

## 4.1 Datasets

To enable systematic evaluation, we introduce a suite of synthetic directed datasets alongside two real-world use cases: (i) neural architecture search, where DAGs model computational pipelines, and (ii) scene graphs, where directed edges encode semantic relations in visual scenes.

**Synthetic datasets** We sample digraphs from four distributions: Erdős–Rényi (binomial model) both general and DAGs variants; Price’s model, a directed analogue of the Barabási–Albert model that produces DAGs; and a directed version of the stochastic block model (SBM) dataset proposed in [46]. Each dataset comprises 200 graphs, split into 128 training, 32 validation, and 40 test graphs.

**TPU Tiles** A relevant application of DAGs is Neural Architecture Search, which aims for an automated design of efficient Neural Networks [18]. For this task, we use the TPU Tiles dataset [54] as a benchmark. It consists of computational graphs extracted from the Tensor Processing Unit workloads. Following [39], we split the data into 5,040 training, 630 validation, and 631 test graphs.

**Visual Genome** Scene graphs structurally represent the semantics of visual scenes, supporting tasks such as image retrieval, captioning, and visual question answering in computer vision and NLP. Our focus is on generating new scene graphs, valuable for tasks such as data augmentation, scenario simulation, or enhancing model robustness, complementing recent work on scene-to-image generation [31, 75]. To accomplish this, we use the Visual Genome dataset [35], a widely adopted benchmark for scene graph-related tasks, providing richly annotated images with object labels, attributes, and pairwise relations. We extract a subset of these graphs, allocating 203 for training, 51 for validation, and 63 for testing. Each graph contains nodes representing objects, relationships, or attributes, each of them spanning several classes. Object nodes represent entities in the scene, relationship nodes mediate directed interactions between pairs of object nodes, and attribute nodes describe properties of individual object nodes.

Further details and statistics for all datasets are available in Appendix E.

## 4.2 Metrics

To evaluate our generations, we build upon the evaluation metrics from the undirected [46, 6] and directed [36] graph generation literature, further extending them to the digraph generative setting.

**Validity, uniqueness, and novelty** For synthetic datasets, assessing *validity* comprises statistical tests to check whether the sampled graphs follow the corresponding generative distribution and, in the case of DAG datasets, ensuring acyclicity. For the TPU Tiles dataset, we measure acyclicity, and, for the Visual Genome dataset, we verify the validation of the typed structural constraints (e.g., edges from relationship nodes can point only to object nodes).

To measure generative diversity while avoiding trivial replication of the training data, we compute the *uniqueness* (fraction of non-isomorphic generated graphs) and *novelty* (fraction of generated graphs not in the training set). The V.U.N. ratio reports the proportion of samples that are simultaneously valid, unique, and novel.

**Distribution alignment** To evaluate proximity to the original distribution, we compute the Maximum Mean Discrepancy (MMD) between generated and test graphs across several graph statistics: incoming and outgoing degree distributions, directed clustering coefficients, spectral features, and wavelet-based features. In particular, spectral features are derived from the directed Laplacian [11]:

$$L = I - \frac{1}{2} \left( \Phi^{\frac{1}{2}} P \Phi^{-\frac{1}{2}} + \Phi^{-\frac{1}{2}} P \Phi^{\frac{1}{2}} \right), \quad (12)$$

where  $P$  is the random walk transition matrix and  $\Phi$  is the diagonal matrix of the Perron vector of  $P$ . This choice simplifies computations compared to alternatives such as the Magnetic Laplacian. We report normalized results as the ratio of statistics from generated samples to those from the training data, allowing for direct comparison. Finally, to summarize these ratios, we average them.

Among all metrics, we consider the aggregated indicators, V.U.N. and the average graph statistics ratio, as the most informative. Additional details on the evaluation metrics are provided in Appendix F.

Table 1: Directed graph generation performance on synthetic graphs for different configurations of DIRECTO. Results are presented as mean  $\pm$  standard deviation across five sampling runs. We considered  $Q = 10$  for the MagLap variants.

Model	Out-degree $\downarrow$	In-degree $\downarrow$	Clustering $\downarrow$	Spectre $\downarrow$	Wavelet $\downarrow$	Ratio $\downarrow$	Valid $\uparrow$	Unique $\uparrow$	Novel $\uparrow$	V.U.N. $\uparrow$
Erdős-Renyi Directed Acyclic Graph (ER-DAG)										
Training set	0.0113	0.0103	0.0355	0.0038	0.0024	1.0	99.2	100	0	0
MLE	0.0083 $\pm$ 0.0004	0.0089 $\pm$ 0.0003	0.1318 $\pm$ 0.0077	0.0823 $\pm$ 0.0013	0.1162 $\pm$ 0.0018	15.1 $\pm$ 0.2	0 $\pm$ 0.0	100 $\pm$ 0.0	100 $\pm$ 0.0	0 $\pm$ 0.0
D-VAE	0.6158 $\pm$ 0.0160	0.6246 $\pm$ 0.0103	1.0509 $\pm$ 0.00304	0.6160 $\pm$ 0.0315	0.5432 $\pm$ 0.0389	106.6 $\pm$ 5.4	0 $\pm$ 0.0	100 $\pm$ 0.0	100 $\pm$ 0.0	0 $\pm$ 0.0
LAYERDAG	0.0750 $\pm$ 0.0697	0.1773 $\pm$ 0.0722	0.1842 $\pm$ 0.0463	0.0159 $\pm$ 0.0120	0.0218 $\pm$ 0.0160	4.2 $\pm$ 3.2	21.5 $\pm$ 2.7	99.9 $\pm$ 0.0	100 $\pm$ 0.0	21.5 $\pm$ 2.7
DIGRESS	0.0138 $\pm$ 0.0035	0.0143 $\pm$ 0.0050	0.1074 $\pm$ 0.0090	0.0073 $\pm$ 0.0017	0.0042 $\pm$ 0.0011	1.9 $\pm$ 0.3	34 $\pm$ 4.1	100 $\pm$ 0.0	100 $\pm$ 0.0	34 $\pm$ 4.1
DEFOG	0.0109 $\pm$ 0.0019	0.0108 $\pm$ 0.0017	0.0540 $\pm$ 0.0112	0.0061 $\pm$ 0.0008	0.0030 $\pm$ 0.0005	1.3 $\pm$ 0.1	67.5 $\pm$ 1.6	100 $\pm$ 0.0	100 $\pm$ 0.0	67.5 $\pm$ 1.6
DIRECTO-DD RRWP	0.0142 $\pm$ 0.0040	0.0129 $\pm$ 0.0034	0.0408 $\pm$ 0.0053	0.0055 $\pm$ 0.0010	0.0048 $\pm$ 0.0014	1.4 $\pm$ 0.3	79 $\pm$ 3.7	100 $\pm$ 0.0	100 $\pm$ 0.0	79 $\pm$ 3.7
DIRECTO-DD MagLap	0.0145 $\pm$ 0.0040	0.0134 $\pm$ 0.0033	0.0582 $\pm$ 0.0083	0.0063 $\pm$ 0.0015	0.0034 $\pm$ 0.0011	1.5 $\pm$ 0.2	85 $\pm$ 9.2	100 $\pm$ 0.0	100 $\pm$ 0.0	85 $\pm$ 9.2
DIRECTO RRWP	0.0107 $\pm$ 0.0019	0.0104 $\pm$ 0.0012	0.1209 $\pm$ 0.0194	0.0054 $\pm$ 0.0005	0.0043 $\pm$ 0.0008	1.7 $\pm$ 0.1	94 $\pm$ 1.0	100 $\pm$ 0.0	100 $\pm$ 0.0	94 $\pm$ 1.0
DIRECTO MagLap	0.0117 $\pm$ 0.0014	0.0110 $\pm$ 0.0015	0.0711 $\pm$ 0.0120	0.0055 $\pm$ 0.0016	0.0026 $\pm$ 0.0004	1.3 $\pm$ 0.2	92 $\pm$ 3.7	100 $\pm$ 0.0	100 $\pm$ 0.0	92 $\pm$ 3.7
Stochastic Bottleneck Model (SBM)										
Training set	0.0031	0.0031	0.0274	0.0027	0.0011	1.0	97.7	100	0	0
MLE	0.0020 $\pm$ 0.0002	0.0020 $\pm$ 0.0002	0.1973 $\pm$ 0.0162	0.0087 $\pm$ 0.0003	0.0508 $\pm$ 0.0009	11.6 $\pm$ 0.2	0 $\pm$ 0.0	100 $\pm$ 0.0	100 $\pm$ 0.0	0 $\pm$ 0.0
DIGRESS	0.0037 $\pm$ 0.0018	0.0038 $\pm$ 0.0018	0.0722 $\pm$ 0.0098	0.0045 $\pm$ 0.0004	0.0142 $\pm$ 0.0039	3.9 $\pm$ 0.9	41.5 $\pm$ 5.1	100 $\pm$ 0.0	100 $\pm$ 0.0	41.5 $\pm$ 5.1
DEFOG	0.0036 $\pm$ 0.0009	0.0034 $\pm$ 0.0008	0.1276 $\pm$ 0.0065	0.0345 $\pm$ 0.0028	0.0961 $\pm$ 0.0071	21.4 $\pm$ 1.6	13.5 $\pm$ 5.4	100 $\pm$ 0.0	100 $\pm$ 0.0	13.5 $\pm$ 5.4
DIRECTO-DD RRWP	0.0036 $\pm$ 0.0019	0.0036 $\pm$ 0.0018	0.0592 $\pm$ 0.0027	0.0038 $\pm$ 0.0007	0.0027 $\pm$ 0.0009	1.7 $\pm$ 0.4	81.5 $\pm$ 3.2	100 $\pm$ 0.0	100 $\pm$ 0.0	81.5 $\pm$ 3.2
DIRECTO-DD MagLap	0.0037 $\pm$ 0.0019	0.0038 $\pm$ 0.0018	0.0450 $\pm$ 0.0037	0.0038 $\pm$ 0.0006	0.0021 $\pm$ 0.0009	1.5 $\pm$ 0.4	95.5 $\pm$ 3.7	100 $\pm$ 0.0	100 $\pm$ 0.0	95.5 $\pm$ 3.7
DIRECTO RRWP	0.0038 $\pm$ 0.0011	0.0037 $\pm$ 0.0012	0.0492 $\pm$ 0.0041	0.0035 $\pm$ 0.0007	0.0015 $\pm$ 0.0004	1.4 $\pm$ 0.2	87 $\pm$ 5.1	100 $\pm$ 0.0	100 $\pm$ 0.0	87 $\pm$ 5.1
DIRECTO MagLap	0.0039 $\pm$ 0.0012	0.0038 $\pm$ 0.0010	0.0654 $\pm$ 0.0052	0.0038 $\pm$ 0.0003	0.0039 $\pm$ 0.0008	2.0 $\pm$ 0.3	96.5 $\pm$ 2.5	100 $\pm$ 0.0	100 $\pm$ 0.0	96.5 $\pm$ 2.5

## 5 Experiments

In this section, we first evaluate the flexibility of our method to generate directed graphs using our newly proposed benchmark, covering two of the synthetic and both real-world datasets. We then analyze the impact of our architectural improvements on generative performance.

**Baselines** In the general directed setting, we compare DIRECTO to a Maximum Likelihood Estimation (MLE) baseline over node count, node types, and edge types. The implementation details are provided in Appendix G.1. For DAG settings, we also include the only two publicly available baselines: D-VAE [77] and LAYERDAG [39].

Notably, the architectural improvements introduced in Secs. 3.2 and 3.3 are agnostic to the underlying graph iterative refinement framework. To demonstrate their versatility and enable for wider experimentation, we extend DIRECTO to a discrete diffusion [67] backbone (DIRECTO-DD). Details of the adopted discrete diffusion formulation are provided in Appendix I.3. We also include as baselines both DEFOG [55] and DIGRESS [67], which are discrete flow matching and discrete diffusion methods designed for the undirected setting, respectively. To make them applicable to the directed setting, we adapt both models by removing their edge symmetrization operations.

For each experiment, we highlight the **best result** and second-best method. Further details on the experimental setup can be found in Appendix G.

### 5.1 Directed Graph Generation Performance

**Synthetic datasets** Table 1 reports the results on two synthetic datasets: ER-DAG and SBM. In both settings, DIRECTO consistently achieves the best trade-off between sample quality and validity. For ER-DAG, it achieves the highest validity score using directed RRWP as positional encoding, with a V.U.N. ratio of 94%. Notably, while LAYERDAG enforces acyclicity by design, it fails to capture the ER structure of the target graph distribution, as evidenced by its low V.U.N. score (21.5%; see Tab. 13 for details). In the SBM case, DIRECTO also successfully captures the distribution and consistently outperforms the baselines, achieving up to 95.5% in V.U.N. ratio and consistently low average graph statistics ratios. In Appendix H, we also provide results for two additional synthetic datasets as well as a study on the effect of dataset size, which shows that larger datasets lead to improved performance but also incur higher computational cost and longer training times.

**Real-world datasets** Table 2 shows the performance for the two real-world datasets. In TPU tiles, all DIRECTO variants significantly outperform DAG generation baselines in terms of structure-aware metrics. The ratio scores for DIRECTO are consistently and substantially lower than those observed in MLE, and especially LayerDAG. This indicates a more realistic distribution. Again, DIRECTO variants achieve higher V.U.N. than all baselines, with the exception of LAYERDAG, which benefits from enforcing acyclicity, the only validity constraint evaluated in this case. For Visual Genome, results reinforce the versatility of DIRECTO. DIRECTO RRWP achieves the highest V.U.N. scores, indicating a superior ability to generate diverse and novel graphs while maintaining structural fidelity.

Table 2: Directed graph generation performance on real-world graphs for different configurations of DIRECTO. Results are presented as mean  $\pm$  standard deviation across five sampling runs. We considered  $Q = 5$  for the MagLap variants. OOT indicates that the model could not be run within a reasonable timeframe. (\*) indicates that isomorphism tests occasionally timed out, due to the large size of some graphs in this dataset; such cases were excluded from the uniqueness computation.

Model	Out-degree $\downarrow$	In-degree $\downarrow$	Clustering $\downarrow$	Spectre $\downarrow$	Wavelet $\downarrow$	Ratio $\downarrow$	Valid $\uparrow$	Unique $\uparrow$	Novel $\uparrow$	V.U.N. $\uparrow$
TPU Tiles										
Training set	0.0003	0.0003	0.0007	0.0006	0.0002	1.0	100	100	0	0
MLE	0.0354 $\pm$ 0.0005	0.0878 $\pm$ 0.0014	0.0141 $\pm$ 0.0006	0.0689 $\pm$ 0.0013	0.0407 $\pm$ 0.0004	149.8 $\pm$ 0.7	24.7 $\pm$ 0.0	99.9 $\pm$ 0.0	100 $\pm$ 0.0	24.7 $\pm$ 0.0
D-VAE	OOT	OOT	OOT	OOT	OOT	OOT	OOT	OOT	OOT	OOT
LAYERDAG	0.1933 $\pm$ 0.0905	0.2225 $\pm$ 0.0395	0.1512 $\pm$ 0.0522	0.0501 $\pm$ 0.0206	0.0765 $\pm$ 0.0251	413.6 $\pm$ 70.1	100 $\pm$ 0.0	99.5 $\pm$ 1.0	98.5 $\pm$ 3.0	98.5 $\pm$ 3.0
DiGRESS	0.0084 $\pm$ 0.0009	0.0726 $\pm$ 0.0019	0.0020 $\pm$ 0.0006	0.0033 $\pm$ 0.0003	0.0018 $\pm$ 0.0003	57.5 $\pm$ 1.7	86.1 $\pm$ 2.3	87.1(*) $\pm$ 5.8	99.4 $\pm$ 0.6	70.9 $\pm$ 3.4
DEFOG	0.0099 $\pm$ 0.0012	0.0794 $\pm$ 0.0023	0.0042 $\pm$ 0.0027	0.0040 $\pm$ 0.0005	0.0017 $\pm$ 0.0003	63.7 $\pm$ 2.6	86.3 $\pm$ 2.2	87.7(*) $\pm$ 5.4	93.3 $\pm$ 2.5	72 $\pm$ 2.4
DIRECTO-DD RRWP	0.0093 $\pm$ 0.0010	0.0767 $\pm$ 0.0035	0.0015 $\pm$ 0.0013	0.0045 $\pm$ 0.0007	0.0018 $\pm$ 0.0005	61.0 $\pm$ 2.9	86.5 $\pm$ 1.9	90.3 $\pm$ 0.8	99.6 $\pm$ 0.5	76.8 $\pm$ 1.9
DIRECTO-DD MagLap	0.0115 $\pm$ 0.0035	0.0703 $\pm$ 0.0033	0.0103 $\pm$ 0.0021	0.0076 $\pm$ 0.0007	0.0043 $\pm$ 0.0014	64.3 $\pm$ 5.3	86.5 $\pm$ 5.1	90.5 $\pm$ 3.3	100 $\pm$ 0.0	77 $\pm$ 7.0
DIRECTO RRWP	0.0133 $\pm$ 0.0025	0.0859 $\pm$ 0.0072	0.0136 $\pm$ 0.0075	0.0086 $\pm$ 0.0010	0.0038 $\pm$ 0.0009	75.4 $\pm$ 8.1	97 $\pm$ 1.0	81.8(*) $\pm$ 4.5	96.5 $\pm$ 1.2	77 $\pm$ 2.9
DIRECTO MagLap	0.0039 $\pm$ 0.0017	0.0376 $\pm$ 0.0051	0.0211 $\pm$ 0.0117	0.0126 $\pm$ 0.0022	0.0062 $\pm$ 0.0009	44.0 $\pm$ 7.1	90.5 $\pm$ 3.3	90.5 $\pm$ 4.6	97.5 $\pm$ 3.2	80.5 $\pm$ 4.6
Visual Genome										
Training set	0.0018	0.0030	0.0000	0.0072	0.0036	1.0	100	100	0	0
MLE	0.0607 $\pm$ 0.0036	0.0474 $\pm$ 0.0023	0.5342 $\pm$ 0.0830	0.0535 $\pm$ 0.0015	0.0399 $\pm$ 0.0017	17.0 $\pm$ 0.6	0 $\pm$ 0.0	100 $\pm$ 0.0	100 $\pm$ 0.0	0 $\pm$ 0.0
DiGRESS	0.0654 $\pm$ 0.0044	0.0389 $\pm$ 0.0032	0.0008 $\pm$ 0.0008	0.0416 $\pm$ 0.0017	0.0225 $\pm$ 0.0007	17.0 $\pm$ 0.6	0.3 $\pm$ 0.6	100 $\pm$ 0.0	100 $\pm$ 0.0	0.3 $\pm$ 0.6
DEFOG	0.0447 $\pm$ 0.0044	0.0396 $\pm$ 0.0028	0.0002 $\pm$ 0.0002	0.0122 $\pm$ 0.0020	0.0089 $\pm$ 0.0011	10.6 $\pm$ 0.8	39.6 $\pm$ 2.8	100 $\pm$ 0.0	100 $\pm$ 0.0	39.6 $\pm$ 2.8
DIRECTO-DD RRWP	0.0424 $\pm$ 0.0043	0.0413 $\pm$ 0.0037	0.0000 $\pm$ 0.0000	0.0132 $\pm$ 0.0053	0.0074 $\pm$ 0.0008	15.3 $\pm$ 0.8	72.7 $\pm$ 3.9	100 $\pm$ 0.0	100 $\pm$ 0.0	72.7 $\pm$ 3.9
DIRECTO-DD MagLap	0.0245 $\pm$ 0.0022	0.0359 $\pm$ 0.0036	0.0000 $\pm$ 0.0000	0.0163 $\pm$ 0.0026	0.0086 $\pm$ 0.0011	7.6 $\pm$ 0.7	86.5 $\pm$ 5.1	100 $\pm$ 0.0	100 $\pm$ 0.0	61.9 $\pm$ 4.4
DIRECTO RRWP	0.0494 $\pm$ 0.0021	0.0425 $\pm$ 0.0029	0.0000 $\pm$ 0.0000	0.0226 $\pm$ 0.0075	0.0228 $\pm$ 0.0058	12.8 $\pm$ 0.6	86 $\pm$ 4.5	98.4 $\pm$ 1.7	99.3 $\pm$ 0.7	83.8 $\pm$ 4.3
DIRECTO MagLap	0.0180 $\pm$ 0.0024	0.0302 $\pm$ 0.0040	0.0000 $\pm$ 0.0000	0.0142 $\pm$ 0.0021	0.0099 $\pm$ 0.0013	6.2 $\pm$ 0.5	67.6 $\pm$ 3.6	99.7 $\pm$ 0.6	99.7 $\pm$ 0.6	67.0 $\pm$ 4.3

## 5.2 Dual Attention Ablation

We now analyze the influence of the dual attention mechanism on the performance of DIRECTO. In Fig. 3, we compare the V.U.N. metric and the average graph statistics ratios ("Ratio") score across both synthetic datasets (ER-DAG and SBM), highlighting the impact of dual attention on generation quality and graph realism. We observe that the dual attention mechanism consistently improves generative performance, regardless of the positional encoding it is combined with. Notably, even in the absence of any positional encoding ("No PE"), dual attention still achieves non-zero V.U.N., highlighting its capacity to independently capture directionality-relevant information. See Appendix H.1 for the full ablation tables, both for DIRECTO and DIRECTO-DD.

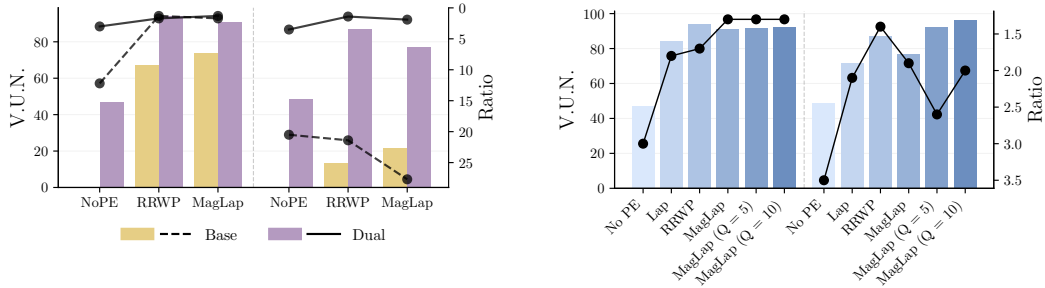


Figure 3: Ablation results for dual attention (left) and positional encodings (right). Each plot shows results on the ER-DAG (left bars/lines) and SBM (right bars/lines) datasets. Better performance corresponds to V.U.N. bars and Ratio lines appearing closer to the top of each subplot.

## 5.3 Positional Encodings Ablation

We also evaluate the sensitivity of DIRECTO to different positional encodings, including a direction-agnostic baseline ("Lap"). In Fig. 3, we observe consistent trends across datasets: integrating positional encodings improves V.U.N. and Ratio, mirroring the undirected setting; moreover, direction-aware encodings outperform agnostic ones, supporting our modeling hypothesis. Among the encodings tested, Directed RRWP achieves the best overall performance on ER-DAG, and MultiMagLapPE with  $Q = 10$  on SBM. Nevertheless, we remark that RRWP demonstrates clear superiority in both scalability and runtime efficiency (see Appendix G.3). Full tables for both DIRECTO and DIRECTO-DD can be found in Appendix H.2.

## 6 Related work

**Graph generative methods** Generative models that were initially adapted to the graph setting include *auto-regressive* methods [76, 41], which grow the graph progressively by inserting nodes and edges, but require node ordering for feasibility. On the other hand, *one-shot* graph generative models such as VAEs [33, 59, 28, 45, 66], GANs [14, 34, 46], and normalizing flows [32, 70, 42, 44] can directly generate full graphs in a single forward pass, thereby eliminating the need for predefined node ordering. Graph diffusion models also belong to this class, with the initial approaches consisting of adaptations of continuous state-space discrete-time diffusion frameworks [61, 25, 62] to the graph setting. These include works such as EDP-GNN [51], DGSM [43], and GeoDiff [73]. Later, the discrete state-space diffusion framework [3] was adopted, with DiGress [67] and MCD [22] operating in discrete time. On the other hand, methods that operate in continuous time [8] were introduced, including GDSS [30] and GruM [29] in continuous state-spaces and DisCo [74] and Cometh [60] for discrete state-spaces. Recent approaches combine the sequential modeling of auto-regressive methods with the global denoising of diffusion [78]. Finally, DeFoG [55] recently achieves state-of-the-art performance by leveraging discrete flow matching [9, 20].

**Directed graph generation** The vast majority of works in this area focus solely on directed acyclic graph (DAG) generation, with research including autoencoders [77], autoregressive methods [38] and, more recently, combining diffusion in different steps of an auto-regressive process [39]. However, they require the input DAGs to be topologically ordered. Other approaches [2, 1] use ideas from discrete diffusion to perform Neural Architecture Search (NAS), but they are tailored to the specific application and, therefore, to DAGs. Finally, the work in [36] is the first to propose a general directed graph generation method, approaching it from an auto-regressive formulation. Unfortunately, to the best of our knowledge, its implementation is not publicly available, which limits its accessibility for study and evaluation.

## 7 Conclusion and future directions

We propose DIRECTO, a novel discrete flow matching-based method for effective directed graph generation. To achieve this, we combine directionality-aware positional encodings with a dual-attention mechanism that explicitly handles source-to-target and target-to-source dependencies. We additionally establish a new benchmarking framework tailored to digraphs, addressing the current lack of standardized evaluation in the field. Empirical results demonstrate that our model significantly outperforms existing baselines in a range of synthetic and real-world datasets. Our approach successfully learns to generate directed structures and preserve critical properties, such as acyclicity, without the need for explicit constraints. Looking forward, scalability, a deeper understanding of the role of permutation equivariance, and further guidance of the generative process remain promising directions of research.

## References

- [1] Sohyun An, Hayeon Lee, Jaehyeong Jo, Seanie Lee, and Sung Ju Hwang. DiffusionNAG: predictor-guided neural architecture generation with diffusion models. *International Conference on Learning Representations*, 2024. [10](#)
- [2] Rohan Asthana, Joshua Conrad, Youssef Dawoud, Maurits Ortmanns, and Vasileios Belagiannis. Multi-conditioned graph diffusion for neural architecture search. *Transactions on Machine Learning Research*, 2024. [10](#)
- [3] Jacob Austin, Daniel D Johnson, Jonathan Ho, Daniel Tarlow, and Rianne Van Den Berg. Structured denoising diffusion models in discrete state-spaces. *Advances in Neural Information Processing Systems*, 34:17981–17993, 2021. [10](#), [34](#)
- [4] Dominique Beaini, Saro Passaro, Vincent Létourneau, Will Hamilton, Gabriele Corso, and Pietro Lió. Directional graph networks. *International Conference on Machine Learning*, 139:748–758, 2021. [4](#)
- [5] Maya Bechler-Speicher, Ben Finkelshtein, Fabrizio Frasca, Luis Müller, Jan Tönshoff, Antoine Siraudin, Viktor Zaverkin, Michael M. Bronstein, Mathias Niepert, Bryan Perozzi, Mikhail Galkin, and Christopher Morris. Position: Graph learning will lose relevance due to poor benchmarks. *International Conference on Machine Learning*, 2025. [6](#)
- [6] Andreas Bergmeister, Karolis Martinkus, Nathanaël Perraudin, and Roger Wattenhofer. Efficient and scalable graph generation through iterative local expansion. *International Conference on Learning Representations*, 2023. [7](#)
- [7] Giorgos Bouritsas, Fabrizio Frasca, Stefanos Zafeiriou, and Michael M. Bronstein. Improving graph neural network expressivity via subgraph isomorphism counting. *IEEE Transactions on Pattern Analysis and Machine Intelligence*, 2020. [4](#)
- [8] Andrew Campbell, Joe Benton, Valentin De Bortoli, Thomas Rainforth, George Deligiannidis, and Arnaud Doucet. A continuous time framework for discrete denoising models. *Advances in Neural Information Processing Systems*, 35:28266–28279, 2022. [10](#)
- [9] Andrew Campbell, Jason Yim, Regina Barzilay, Tom Rainforth, and Tommi Jaakkola. Generative flows on discrete state-spaces: Enabling multimodal flows with applications to protein co-design. *International Conference on Machine Learning*, 213:5453 – 5512, 2024. [3](#), [10](#), [19](#), [33](#)
- [10] Xiaojun Chang, Pengzhen Ren, Pengfei Xu, Zhihui Li, Xiaojiang Chen, and Alex Hauptmann. A comprehensive survey of scene graphs: Generation and application. *IEEE Transactions on Pattern Analysis and Machine Intelligence*, 45(1):1–26, 2023. [1](#)
- [11] Fan Chung. Laplacians and the cheeger inequality for directed graphs. *Annals of Combinatorics*, 9:1–19, 2005. [7](#)
- [12] Anna Concas, Caterina Fenu, Lothar Reichel, Giuseppe Rodriguez, and Yunzi Zhang. Chained structure of directed graphs with applications to social and transportation networks. *Applied Network Science*, 7(1), 2022. [1](#)
- [13] Gabriele Corso, Luca Cavalleri, Dominique Beaini, Pietro Lió, and Petar Veličković. Principal neighbourhood aggregation for graph nets. *Advances in Neural Information Processing Systems*, 33:13260–13271, 2020. [6](#), [17](#)
- [14] Nicola De Cao and Thomas Kipf. MolGAN: An implicit generative model for small molecular graphs. *ICML Workshop on Theoretical Foundations and Applications of Deep Generative Models*, 2018. [10](#)
- [15] Derek J. de Solla Price. Networks of scientific papers. *Science*, 149(3683):510–515, 1965. [21](#)
- [16] Vijay Prakash Dwivedi and Xavier Bresson. A generalization of transformer networks to graphs. *AAAI Workshop on Deep Learning on Graphs: Methods and Applications*, 2021. [5](#), [33](#)
- [17] Floor Eijkelboom, Grigory Bartosh, Christian Andersson Naesseth, Max Welling, and Jan-Willem van de Meent. Variational flow matching for graph generation. *Advances in Neural Information Processing Systems*, 37:11735–11764, 2024. [1](#)
- [18] Thomas Elsken, Jan Hendrik Metzen, and Frank Hutter. Neural architecture search: A survey. *Journal of Machine Learning Research*, 20(55):1–21, 2019. [7](#)
- [19] Paul Erdős and Alfred Rényi. On random graphs I. *Publ. math. debrecen*, 6(290-297):18, 1959. [21](#)

- [20] Itai Gat, Tal Remez, Neta Shaul, Felix Kreuk, Ricky T. Q. Chen, Gabriel Synnaeve, Yossi Adi, and Yaron Lipman. Discrete flow matching. *Advances in Neural Information Processing Systems*, 37:133345–133385, 2024. [3](#), [10](#), [33](#)
- [21] Simon Geisler, Yujia Li, Daniel J Mankowitz, Ali Taylan Cemgil, Stephan Günnemann, and Cosmin Paduraru. Transformers meet directed graphs. *International Conference on Machine Learning*, 447:11144–11172, 2023. [4](#), [5](#), [18](#)
- [22] Kilian Konstantin Haefeli, Karolis Martinkus, Nathanael Perraudin, and Roger Wattenhofer. Diffusion models for graphs benefit from discrete state spaces. *NeurIPS Workshop on New Frontiers in Graph Learning*, 2022. [10](#)
- [23] Frank Harary and Edgar M. Palmer. *Graphical Enumeration*. Academic Press, 1973. [2](#)
- [24] Leonhard Held and Daniel Sabanés Bové. *Applied Statistical Inference: Likelihood and Bayes*. Springer Publishing Company, Incorporated, 2013. [23](#)
- [25] Jonathan Ho, Ajay Jain, and Pieter Abbeel. Denoising diffusion probabilistic models. *Advances in Neural Information Processing Systems*, 33:6840–6851, 2020. [10](#)
- [26] Paul W. Holland, Kathryn Blackmond Laskey, and Samuel Leinhardt. Stochastic blockmodels: First steps. *Social Networks*, 5(2):109–137, 1983. [21](#)
- [27] Yinan Huang, Haoyu Wang, and Pan Li. What are good positional encodings for directed graphs? *International Conference on Learning Representations*, 2025. [4](#), [18](#)
- [28] Wengong Jin, Regina Barzilay, and Tommi Jaakkola. Junction tree variational autoencoder for molecular graph generation. *International Conference on Machine Learning*, pages 2323–2332, 2018. [10](#)
- [29] Jaehyeong Jo, Dongki Kim, and Sung Ju Hwang. Graph generation with diffusion mixture. *International Conference on Machine Learning*, 900:22371 – 22405, 2024. [10](#)
- [30] Jaehyeong Jo, Seul Lee, and Sung Ju Hwang. Score-based generative modeling of graphs via the system of stochastic differential equations. *International Conference on Machine Learning*, pages 10362–10383, 2022. [10](#)
- [31] Justin Johnson, Agrim Gupta, and Li Fei-Fei. Image generation from scene graphs. *IEEE Conference on Computer Vision and Pattern Recognition*, pages 1219–1228, 2018. [7](#)
- [32] Madhava Kaushalya, Ishiguro Katushiko, Nakago Kosuke, and Abe Motoki. GraphNVP: An invertible flow model for generating molecular graphs. *arXiv preprint arXiv:1905.11600*, 2019. [10](#)
- [33] Thomas N. Kipf and Max Welling. Variational graph auto-encoders. *NeurIPS Workshop on Bayesian Deep Learning*, 2016. [10](#)
- [34] Igor Krawczuk, Pedro Abranches, Andreas Loukas, and Volkan Cevher. GG-GAN: A geometric graph generative adversarial network. *OpenReview*, 2021. [10](#)
- [35] Ranjay Krishna, Yuke Zhu, Oliver Groth, Justin Johnson, Kenji Hata, Joshua Kravitz, Stephanie Chen, Yannis Kalantidis, Li-Jia Li, David A Shamma, et al. Visual genome: Connecting language and vision using crowdsourced dense image annotations. *International Journal of Computer Vision*, 123:32–73, 2017. [2](#), [7](#), [22](#)
- [36] Marc T. Law, Karsten Kreis, and Haggai Maron. Directed graph generation with heat kernels. *Transactions on Machine Learning Research*, 2025. [1](#), [7](#), [10](#), [24](#)
- [37] Chun Li, Nannan Tang, and Jun Wang. Directed graphs of dna sequences and their numerical characterization. *Journal of Theoretical Biology*, 241(2):173–177, 2006. [1](#)
- [38] Muchen Li, Jeffrey Yunfan Liu, Leonid Sigal, and Renjie Liao. GraphPNAS: learning distribution of good neural architectures via deep graph generative models. *arXiv preprint arXiv:2211.15155*, 2022. [10](#)
- [39] Mufei Li, Viraj Shitole, Eli Chien, Changhai Man, Zhaodong Wang, Srinivas Sridharan, Ying Zhang, Tushar Krishna, and Pan Li. LayerDAG: A layerwise autoregressive diffusion model for directed acyclic graph generation. *International Conference on Learning Representations*, 2025. [1](#), [2](#), [7](#), [8](#), [10](#), [21](#), [25](#)
- [40] Xujia Li, Yuan Li, Xueying Mo, Hebing Xiao, Yanyan Shen, and Lei Chen. Diga: Guided diffusion model for graph recovery in anti-money laundering. *ACM SIGKDD Conference on Knowledge Discovery and Data Mining*, page 4404–4413, 2023. [1](#)

- [41] Renjie Liao, Yujia Li, Yang Song, Shenlong Wang, Charlie Nash, William L. Hamilton, David Duvenaud, Raquel Urtasun, and Richard Zemel. Efficient graph generation with graph recurrent attention networks. *Advances in Neural Information Processing Systems*, 383:4255 – 4265, 2019. [1](#), [10](#)
- [42] Phillip Lippe and Efstratios Gavves. Categorical normalizing flows via continuous transformations. *International Conference on Learning Representations*, 2021. [10](#)
- [43] Shitong Luo, Chence Shi, Minkai Xu, and Jian Tang. Predicting molecular conformation via dynamic graph score matching. *Advances in Neural Information Processing Systems*, 34:19784–19795, 2021. [10](#)
- [44] Youzhi Luo, Keqiang Yan, and Shuiwang Ji. GraphDF: A discrete flow model for molecular graph generation. *International Conference on Machine Learning*, 139:7192–7203, 2021. [10](#)
- [45] Changsheng Ma and Xiangliang Zhang. GF-VAE: A flow-based variational autoencoder for molecule generation. *ACM International Conference on Information & Knowledge Management*, page 1181–1190, 2021. [10](#)
- [46] Karolis Martinkus, Andreas Loukas, Nathanaël Perraudin, and Roger Wattenhofer. SPECTRE: Spectral conditioning helps to overcome the expressivity limits of one-shot graph generators. *International Conference on Machine Learning*, 162:15159–15179, 2022. [1](#), [7](#), [10](#), [24](#), [25](#)
- [47] Rocío Mercado, Tobias Rastemo, Edvard Lindelöf, Günter Klambauer, Ola Engkvist, Hongming Chen, and Esben Jannik Bjerrum. Graph Networks for Molecular Design. *Machine Learning: Science and Technology*, 2020. [1](#)
- [48] Christopher Morris, Martin Ritzert, Matthias Fey, William L. Hamilton, Jan Eric Lenssen, Gaurav Rattan, and Martin Grohe. Weisfeiler and Leman go neural: Higher-order graph neural networks. *AAAI Conference on Artificial Intelligence*, 2019. [4](#)
- [49] Alexander Quinn Nichol and Prafulla Dhariwal. Improved denoising diffusion probabilistic models. *International Conference on Machine Learning*, 574:6840 – 6851, 2021. [34](#)
- [50] Giannis Nikolentzos, Michalis Vazirgiannis, Christos Xypolopoulos, Markus Lingman, and Erik G. Brandt. Synthetic electronic health records generated with variational graph autoencoders. *Digital Medicine*, 6(1):83, 2023. [1](#)
- [51] Chenhao Niu, Yang Song, Jiaming Song, Shengjia Zhao, Aditya Grover, and Stefano Ermon. Permutation invariant graph generation via score-based generative modeling. *International Conference on Artificial Intelligence and Statistics*, pages 4474–4484, 2020. [10](#)
- [52] Tiago P. Peixoto. Efficient monte carlo and greedy heuristic for the inference of stochastic block models. *Physical Review E*, 89(1), 2014. [23](#)
- [53] Ethan Perez, Florian Strub, Harm De Vries, Vincent Dumoulin, and Aaron Courville. FiLM: Visual reasoning with a general conditioning layer. *AAAI Conference on Artificial Intelligence*, 32-1:3942 – 3951, 2018. [6](#)
- [54] Pithchaya Mangpo Phothilimthana, Sami Abu-El-Haija, Kaidi Cao, Bahare Fatemi, Michael Burrows, Charith Mendis, and Bryan Perozzi. TpuGraphs: A performance prediction dataset on large tensor computational graphs. *Advances on Neural Information Processing Systems (Datasets and Benchmarks Track)*, 2023. [2](#), [7](#), [21](#)
- [55] Yiming Qin, Manuel Madeira, Dorina Thanou, and Pascal Frossard. DeFoG: Discrete flow matching for graph generation. *International Conference on Machine Learning*, 2025. [1](#), [3](#), [4](#), [6](#), [8](#), [10](#), [19](#), [26](#), [32](#), [33](#)
- [56] Ladislav Rampásek, Michael Galkin, Vijay Prakash Dwivedi, Anh Tuan Luu, Guy Wolf, and Dominique Beaini. Recipe for a general, powerful, scalable graph transformer. *Advances in Neural Information Processing Systems*, 35:14501–14515, 2022. [5](#)
- [57] Ivan Rodin, Antonino Furnari, Kyle Min, Subarna Tripathi, and Giovanni Maria Farinella. Action scene graphs for long-form understanding of egocentric videos. *IEEE Conference on Computer Vision and Pattern Recognition*, pages 18622–18632, 2023. [1](#)
- [58] Christoph Schweimer, Christine Gfrerer, Florian Lugstein, David Pape, Jan A Velimsky, Robert Elsässer, and Bernhard C Geiger. Generating simple directed social network graphs for information spreading. *ACM Web Conference 2022*, pages 1475–1485, 2022. [1](#)
- [59] Martin Simonovsky and Nikos Komodakis. GraphVAE: Towards generation of small graphs using variational autoencoders. *arXiv preprint arXiv:1802.03480*, 2018. [10](#)

- [60] Antoine Siraudin, Fragkiskos D Malliaros, and Christopher Morris. Cometh: A continuous-time discrete-state graph diffusion model. *arXiv preprint arXiv:2406.06449*, 2024. 1, 3, 4, 6, 10, 32
- [61] Jascha Sohl-Dickstein, Eric Weiss, Niru Maheswaranathan, and Surya Ganguli. Deep unsupervised learning using nonequilibrium thermodynamics. *International Conference on Machine Learning*, 37:2256–2265, 2015. 10
- [62] Jiaming Song, Chenlin Meng, and Stefano Ermon. Denoising diffusion implicit models. *International Conference on Learning Representations*, 2021. 10
- [63] Henan Sun, Xunkai Li, Daohan Su, Junyi Han, Rong-Hua Li, and Guoren Wang. Towards data-centric machine learning on directed graphs: a survey. *arXiv preprint arXiv:2412.01849*, 2024. 6
- [64] Martha Takane, Saúl Bernal-González, Jesús Mauro-Moreno, Gustavo García-López, Bruno Méndez-Ambrosio, and Francisco F De-Miguel. Directed graph theory for the analysis of biological regulatory networks. *bioRxiv preprint bioRxiv:2023.10.02.560622*, 2023. 1
- [65] Jui-Yi Tsai, Ya-Wen Teng, Ho Chiok Yew, De-Nian Yang, and Lydia Y. Chen. CDGraph: Dual conditional social graph synthesizing via diffusion model. *arXiv preprint arXiv:2311.01729*, 2023. 1
- [66] Clement Vignac and Pascal Frossard. Top-N: Equivariant set and graph generation without exchangeability. *International Conference on Learning Representations*, 2022. 10
- [67] Clement Vignac, Igor Krawczuk, Antoine Siraudin, Bohan Wang, Volkan Cevher, and Pascal Frossard. DiGress: Discrete denoising diffusion for graph generation. *International Conference on Learning Representations*, 2023. 1, 3, 4, 6, 8, 10, 26, 32, 34
- [68] Clement Vignac, Nagham Osman, Laura Toni, and Pascal Frossard. MiDi: Mixed graph and 3d denoising diffusion for molecule generation. *European Conference on Machine Learning*, pages 560 – 576, 2023. 1
- [69] Qitong Wang, Georgios Kollias, Vasileios Kalantzis, Naoki Abe, and Mohammed J Zaki. Directed graph transformers. *Transactions on Machine Learning Research*, 2024. 5
- [70] Antoine Wehenkel and Gilles Louppe. Graphical normalizing flows. *International Conference on Artificial Intelligence and Statistics*, 130:37–45, 2021. 10
- [71] Pi-Jing Wei, Ziqiang Guo, Zhen Gao, Zheng Ding, Rui-Fen Cao, Yansen Su, and Chun-Hou Zheng. Inference of gene regulatory networks based on directed graph convolutional networks. *Briefings in Bioinformatics*, 25(4), 2024. 1
- [72] Keyulu Xu, Weihua Hu, Jure Leskovec, and Stefanie Jegelka. How powerful are graph neural networks? *International Conference on Learning Representations*, 2019. 4
- [73] Minkai Xu, Lantao Yu, Yang Song, Chence Shi, Stefano Ermon, and Jian Tang. Geodiff: A geometric diffusion model for molecular conformation generation. *International Conference on Learning Representations*, 2022. 10
- [74] Zhe Xu, Ruizhong Qiu, Yuzhong Chen, Huiyuan Chen, Xiran Fan, Menghai Pan, Zhichen Zeng, Mahashweta Das, and Hanghang Tong. Discrete-state continuous-time diffusion for graph generation. *Advances on Neural Information Processing Systems*, 2531:79704 – 79740, 2024. 1, 3, 4, 10, 32
- [75] Ling Yang, Zhilin Huang, Yang Song, Shenda Hong, Guohao Li, Wentao Zhang, Bin Cui, Bernard Ghanem, and Ming-Hsuan Yang. Diffusion-based scene graph to image generation with masked contrastive pre-training. *arXiv preprint arXiv:2211.11138*, 2022. 7
- [76] Jiaxuan You, Rex Ying, Xiang Ren, William L. Hamilton, and Jure Leskovec. GraphRNN: Generating realistic graphs with deep auto-regressive models. *International Conference on Machine Learning*, 80:5694–5703, 2018. 10
- [77] Muhan Zhang, Shali Jiang, Zhicheng Cui, Roman Garnett, and Yixin Chen. D-VAE: A variational autoencoder for directed acyclic graphs. *Advances in Neural Information Processing Systems*, 142:1588–1600, 2019. 1, 8, 10, 25
- [78] Lingxiao Zhao, Xueying Ding, and Leman Akoglu. Pard: Permutation-invariant autoregressive diffusion for graph generation. *Advances in Neural Information Processing Systems*, 37:7156–7184, 2024. 10

# Appendix

## Table of Contents

---

<b>A</b>	<b>Dual Attention</b>	<b>16</b>
<b>B</b>	<b>Positional Encodings</b>	<b>17</b>
<b>C</b>	<b>Sampling Optimization in DIRECTO</b>	<b>19</b>
<b>D</b>	<b>DIRECTO Training and Sampling Algorithms</b>	<b>20</b>
<b>E</b>	<b>Dataset descriptions</b>	<b>20</b>
E.1	Synthetic datasets . . . . .	21
E.2	TPU Tiles . . . . .	21
E.3	Visual Genome . . . . .	22
<b>F</b>	<b>Further details on evaluation metrics</b>	<b>22</b>
F.1	Validity metrics . . . . .	23
F.2	Uniqueness and novelty . . . . .	24
F.3	Maximum Mean Discrepancy metrics . . . . .	24
<b>G</b>	<b>Experimental details</b>	<b>25</b>
G.1	Details on baselines . . . . .	25
G.2	Training setup . . . . .	26
G.3	Resources and runtime . . . . .	27
<b>H</b>	<b>Additional results</b>	<b>27</b>
H.1	The role of dual attention . . . . .	28
H.2	The role of positional encodings . . . . .	29
H.3	ER vs DAG performance . . . . .	30
H.4	Effect of dataset size . . . . .	30
H.5	Impact of sampling optimization using discrete flow matching . . . . .	31
<b>I</b>	<b>Iterative Refinement Methods for Graph Generation</b>	<b>32</b>
I.1	Graph iterative refinement methods . . . . .	32
I.2	Discrete flow matching for graph generation . . . . .	33
I.3	Discrete diffusion for graph generation . . . . .	34
<b>J</b>	<b>Visualizations</b>	<b>35</b>
<b>K</b>	<b>Impact statement and limitations</b>	<b>41</b>

---

## A Dual Attention

In this section, we provide a detailed description of the dual attention mechanism used in our model, which effectively integrates both target-to-source and source-to-target information to enhance the graph generation process.

We start with the stacked tensors of node  $\mathbf{X} \in \mathbb{R}^{B \times N \times d_x}$ , edge  $\mathbf{E} \in \mathbb{R}^{B \times N \times N \times d_e}$  and global  $\mathbf{y} \in \mathbb{R}^{B \times d_y}$  features, where  $B$  is the batch size,  $N$  is the number of nodes of the biggest graph in the batch, and  $d_x$ ,  $d_e$ , and  $d_y$  are the node, edge, and global feature dimensions respectively. To handle different node sizes in a batch, we use a binary node mask  $\mathbf{M} \in \{0, 1\}^{B \times N \times 1}$  that accounts for the presence of nodes in each graph.

First, we begin by projecting the queries, keys, and values for the source and the target directions. These are then projected and reshaped into  $n_h$  heads of dimension  $d_q = d_x/n_h$ , thus obtaining for each node:

$$\mathbf{Q}_S = \text{reshape}(\mathbf{M} \odot \mathbf{W}_Q^S \mathbf{X}), \quad \mathbf{K}_S = \text{reshape}(\mathbf{M} \odot \mathbf{W}_K^S \mathbf{X}), \quad \mathbf{V}_S = \text{reshape}(\mathbf{M} \odot \mathbf{W}_V^S \mathbf{X}), \quad (13)$$

$$\mathbf{Q}_T = \text{reshape}(\mathbf{M} \odot \mathbf{W}_Q^T \mathbf{X}), \quad \mathbf{K}_T = \text{reshape}(\mathbf{M} \odot \mathbf{W}_K^T \mathbf{X}), \quad \mathbf{V}_T = \text{reshape}(\mathbf{M} \odot \mathbf{W}_V^T \mathbf{X}), \quad (14)$$

where  $\mathbf{W}_Q^S, \mathbf{W}_K^S, \mathbf{W}_V^S, \mathbf{W}_Q^T, \mathbf{W}_K^T, \mathbf{W}_V^T$  are the learned linear projections. The final shape of each of the elements after the reshaping is  $B \times N \times n_h \times d_q$ .

Then we compute the dual attention, both from source to target and from target to source:

$$\mathbf{Y}_{ST}[i, j] = \frac{\mathbf{Q}_S[i] \cdot \mathbf{K}_T[j]}{\sqrt{d_q}}, \quad \mathbf{Y}_{TS}[i, j] = \frac{\mathbf{Q}_T[i] \cdot \mathbf{K}_S[j]}{\sqrt{d_q}}. \quad (15)$$

with  $i, j$  the index nodes and each  $\mathbf{Y} \in \mathbb{R}^{B \times N \times N \times n_h \times d_q}$ .

To incorporate edge features into the attention mechanism, we apply FiLM-style modulation using additive and multiplicative projections  $\mathbf{W}_{\text{mul}}, \mathbf{W}_{\text{add}}$ :

$$\mathbf{E}_{\text{mul}}^S = \text{reshape}(\mathbf{W}_{\text{mul}}^S(\mathbf{E})), \quad \mathbf{E}_{\text{add}}^S = \text{reshape}(\mathbf{W}_{\text{add}}^S(\mathbf{E})), \quad (16)$$

$$\mathbf{E}_{\text{mul}}^T = \text{reshape}(\mathbf{W}_{\text{mul}}^T(\mathbf{E}^\top)), \quad \mathbf{E}_{\text{add}}^T = \text{reshape}(\mathbf{W}_{\text{add}}^T(\mathbf{E}^\top)), \quad (17)$$

where we reshape the edge features to  $\mathbf{E} \in \mathbb{R}^{B \times N \times N \times n_h \times d_e}$ . This is done so that they can be added or multiplied to the attention scores  $\mathbf{Y}_{ST}$  and  $\mathbf{Y}_{TS}$  to modify them:

$$\mathbf{Y}_{ST} \leftarrow \mathbf{Y}_{ST} \cdot (\mathbf{E}_{\text{mul}}^S + 1) + \mathbf{E}_{\text{add}}^S, \quad (18)$$

$$\mathbf{Y}_{TS} \leftarrow \mathbf{Y}_{TS} \cdot (\mathbf{E}_{\text{mul}}^T + 1) + \mathbf{E}_{\text{add}}^T. \quad (19)$$

**Edge Feature Update** To get the final update of the edge features, the attention-weighted edge representations are flattened and modulated by global features  $\mathbf{y}$  using FiLM with additive and multiplicative projections  $\mathbf{W}_{\text{add}}^E$  and  $\mathbf{W}_{\text{mul}}^E$ :

$$\mathbf{E}' = \mathbf{W}_{\text{add}}^E(\mathbf{y}) + (\mathbf{W}_{\text{mul}}^E(\mathbf{y}) + 1) \odot \text{flatten}(\mathbf{Y}_{ST}), \quad (20)$$

where we flatten over the last dimension. We use  $\mathbf{Y}_{ST}$  as it captures the directional flow from source to target, avoiding ambiguity in the directional influence, and still effectively encoding the influence of source nodes on their targets. Then, the result is followed by an output projection and a residual connection

$$\mathbf{E}' = \mathbf{W}_{\text{out}}^E(\mathbf{E}'), \quad \mathbf{E}' \leftarrow \mathbf{E} + \mathbf{E}', \quad (21)$$

resulting in the updated  $\mathbf{E}' \in \mathbb{R}^{B \times N \times N \times d_e}$ .

**Node Feature Update** To perform the node feature update, first we concatenate the dual attention scores and apply softmax:

$$\mathbf{A}_{\text{aggr}} = \text{softmax}(\text{concat}(\mathbf{Y}_{ST}, \mathbf{Y}_{TS})) \in \mathbb{R}^{B \times N \times 2N \times n_h \times d_e}, \quad (22)$$

$$\mathbf{V}_{\text{aggr}} = \text{concat}(\mathbf{V}_T, \mathbf{V}_T) \in \mathbb{R}^{B \times 2N \times n_h \times d_x}, \quad (23)$$

with  $\text{concat}()$  being the concatenation over the third dimension for  $\mathbf{A}_{\text{aggr}}$  and over the second dimension for  $\mathbf{V}_{\text{aggr}}$ .

After this, the unified weights are aggregated through weighted summation and the result flattened over the second dimension to produce:

$$\mathbf{X}_{\text{aggr}} = \text{attn}_{\text{aggr}} \mathbf{V}_{\text{aggr}} \in \mathbb{R}^{B \times N \times n_h \times d_x}. \quad (24)$$

We then FiLM-modulate the attended features with the global vector  $\mathbf{y}$  with additive and multiplicative projections  $\mathbf{W}_{\text{add}}^X$  and  $\mathbf{W}_{\text{mul}}^X$  to produce:

$$\mathbf{X}_{\text{mod}} = \mathbf{W}_{\text{add}}^X(\mathbf{y}) + (\mathbf{W}_{\text{mul}}^X(\mathbf{y}) + 1) \odot \mathbf{X}_{\text{aggr}}, \quad (25)$$

To allow the model to adaptively balance between preserving the original node features and incorporating the updated ones, we introduce a learnable gating mechanism  $\mathbf{g}_X \in [0, 1]$ :

$$\mathbf{g}_X = \sigma(\mathbf{W}_{\text{gate}}^X \odot \text{concat}(\mathbf{X}, \mathbf{V}_{\text{aggr}})), \quad (26)$$

followed by a gated residual connection:

$$\mathbf{X}' = (1 + \mathbf{g}_X) \odot \mathbf{X} + (1 - \mathbf{g}_X) \odot \mathbf{X}_{\text{mod}}, \quad (27)$$

where the weights assigned to  $\mathbf{X}$  and  $\mathbf{X}_{\text{mod}}$  sum up to 2, ensuring that the overall magnitude remains consistent with the ungated case.

Finally, the result is followed by an output projection:

$$\mathbf{X}' = \mathbf{W}_{\text{out}}^X(\mathbf{X}'), \quad (28)$$

resulting in the updated  $\mathbf{X}' \in \mathbb{R}^{B \times N \times d_x}$ .

**Global Features Update** The updated global vector is computed by aggregating from the node  $\mathbf{X}$  and edge  $\mathbf{E}$  projections:

$$\mathbf{y}' = \mathbf{y} + W_y(\mathbf{y}) + X_{\rightarrow y}(\mathbf{X}) + E_{\rightarrow y}(\mathbf{E}), \quad (29)$$

where  $X_{\rightarrow y}$  and  $E_{\rightarrow y}$  are PNA layers [13] that given node features  $\mathbf{X} \in \mathbb{R}^{B \times N \times d_x}$  or edge features  $\mathbf{E} \in \mathbb{R}^{B \times N \times N \times d_e}$  and a learnable weight matrix  $\mathbf{W}_{\text{PNA}}$ , computes

$$\text{PNA}(\mathbf{X}) = \text{concat}(\max(\mathbf{X}), \min(\mathbf{X}), \text{mean}(\mathbf{X}), \text{std}(\mathbf{X})) \mathbf{W}_{\text{PNA}} \in \mathbb{R}^{4d_x}, \quad (30)$$

$$\text{PNA}(\mathbf{E}) = \text{concat}(\max(\mathbf{E}), \min(\mathbf{E}), \text{mean}(\mathbf{E}), \text{std}(\mathbf{E})) \mathbf{W}_{\text{PNA}} \in \mathbb{R}^{4d_e}, \quad (31)$$

where the different operations are performed over the features and then concatenation is performed along the feature dimension. Both results then pass through a linear layer resulting in  $X_{\rightarrow y}(\mathbf{X}), E_{\rightarrow y}(\mathbf{E}) \in \mathbb{R}^{d_y}$ .

Once again, we use an output projection

$$\mathbf{y}' = \mathbf{W}_{\text{out}}^y(\mathbf{y}'), \quad (32)$$

which results in the updated global features  $\mathbf{y}' \in \mathbb{R}^{B \times d_y}$ .

This dual attention block is applied  $L$  times within the graph transformer.

## B Positional Encodings

To effectively capture the structural properties of directed graphs, we explore a range of positional encodings (PEs) that can be incorporated into the transformer architecture. These encodings provide nodes with a sense of position and orientation within the digraph, enabling the model to better reason about directionality. Below, we detail the specific PEs evaluated in our work.

**Laplacian (Lap)** Traditionally in the undirected case, the eigenvectors of the combinatorial Laplacian are widely used to encode graph structure, relying on the spectral decomposition  $\mathbf{L} = \mathbf{\Gamma} \mathbf{\Lambda} \mathbf{\Gamma}^{-1}$  where  $\mathbf{L}$  is the combinatorial Laplacian,  $\mathbf{\Lambda}$  is the diagonal matrix of eigenvalues, and  $\mathbf{\Gamma}$  is the matrix of eigenvectors. The unnormalized and normalized Laplacians are defined as

$$\mathbf{L}_U = \mathbf{D} - \mathbf{A}_s, \quad \mathbf{L}_N = \mathbf{I} - \mathbf{D}^{-1/2} \mathbf{A}_s \mathbf{D}^{-1/2}, \quad (33)$$

where  $\mathbf{A}_s$  is the adjacency matrix (symmetrized when working with digraphs) and  $\mathbf{D}$  is the degree matrix. However, when dealing with directed graphs, this symmetrization discards directionality information, as it enforces  $\mathbf{A}_s = \mathbf{A}_s^T$ , but it is necessary to guarantee that  $\mathbf{L}_U$  and  $\mathbf{L}_N$  are symmetric and positive semi-definite.

**Magnetic Laplacian (MagLap)** To retain directional information while preserving desirable spectral properties, authors in [21] propose the *Magnetic Laplacian*, which introduces a complex-valued phase encoding into the adjacency matrix. Specifically, the (unnormalized and normalized) Magnetic Laplacians are given by:

$$\mathbf{L}_{\text{dir},U}^{(q)} = \mathbf{D} - (\mathbf{A}_s \odot \exp(i\Theta^{(q)})), \quad \mathbf{L}_{\text{dir},N}^{(q)} = \mathbf{I} - \left( (\mathbf{D}^{-1/2} \mathbf{A}_s \mathbf{D}^{-1/2}) \odot \exp(i\Theta^{(q)}) \right), \quad (34)$$

where  $\odot$  denotes the element-wise (Hadamard) product,  $i$  is the imaginary unit, and the phase matrix  $\Theta^{(q)}$  is defined as:

$$\Theta_{u,v}^{(q)} = 2\pi q (\mathbf{A}_{u,v} - \mathbf{A}_{v,u}). \quad (35)$$

The potential parameter  $q \geq 0$  controls the strength of the phase shift. For  $q = 0$ , the Magnetic Laplacian reduces to the classical combinatorial Laplacian. The resulting complex-valued eigenvectors can effectively encode directionality patterns in the graph. We leverage the information by concatenating the real and complex parts of the eigenvectors to the node features, and the eigenvalues to the global graph features.

**Multi- $q$  Magnetic Laplacian** Recent work by [27] extends the Magnetic Laplacian by introducing a multi- $q$  formulation, which considers as positional encoding stacking together the eigenvalues and eigenvectors of  $Q$  distinct Magnetic Laplacians with potentials  $q_1, \dots, q_Q$ . This approach enables the recovery of the bidirectional walk profile, a generalization of walk counting in undirected graphs that captures a broader range of directional relationships.

By incorporating information from multiple potentials, the multi- $q$  formulation enhances the representational power for directed structures. In particular, they show that the method is robust to the chosen potentials  $q$  chosen. In our model, we leverage this information by concatenating the first  $k$  eigenvectors (real and imaginary parts) of each of the  $Q$  magnetic Laplacians to the global features, and the corresponding first  $k$  eigenvalues to the node features, providing direction-aware structural signals to both levels of representation. As a drawback, this positional encoding results in higher computational costs, as it is necessary to compute several eigenvalue decompositions and, in addition, results in a higher dimensional positional encoding to be processed by the denoising network.

**Directed Relative Random Walk Probabilities (RRWP)** For undirected graphs, RRWP encodes the likelihood of arriving from one node to another through  $k$ -step random walks. This is usually expressed via a transition matrix  $\mathbf{T}^k$ , with  $\mathbf{T} = \mathbf{A}\mathbf{D}^{-1}$ , that encodes the transition probabilities.

For directed graphs, it is possible to consider  $\mathbf{T} = \mathbf{A}\mathbf{D}_{\text{out}}^{-1}$ , where we take into account the degree matrix of the outgoing edges  $\mathbf{D}_{\text{out}}^{-1}$  [21]. The  $K$ -step transition probabilities are then captured by powers of  $\mathbf{T}$ , producing the sequence  $[\mathbf{I}, \mathbf{T}, \mathbf{T}^2, \dots, \mathbf{T}^{K-1}]$ .

Additionally, in the directed setting, authors in [21] suggest it is also informative to model reverse random walks, starting from incoming edges. For this, we can define the reverse transition matrix  $\mathbf{R} = \mathbf{A}^\top \mathbf{D}_{\text{in}}^{-1}$ , where  $\mathbf{D}_{\text{in}}$  is the in-degree matrix. This would represent the likelihood of arriving at a given edge starting from another through  $k$ -step random walks. Analogously, we compute  $[\mathbf{I}, \mathbf{R}, \mathbf{R}^2, \dots, \mathbf{R}^{K-1}]$ .

To have our final positional encoding, following [21], we ensure that graphs are not nilpotent and that the probabilities encoded in the matrices sum up to 1 by adding self-loops to sink nodes during pre-processing. Finally, the full positional encoding concatenates both forward and reverse walk features for a pre-defined  $K$ , yielding:

$$\text{RRPW}(G) = [\mathbf{I}, \mathbf{T}, \mathbf{T}^2, \dots, \mathbf{T}^{K-1}, \mathbf{I}, \mathbf{R}, \mathbf{R}^2, \dots, \mathbf{R}^{K-1}]. \quad (36)$$

We concatenate the PE to the edge features, and additionally concatenate the diagonal elements of each matrix to the node features to further infuse them with the information.

Additionally, to mitigate that for large  $k$  the probabilities tend to converge to sink nodes, we optionally incorporate *Personalized PageRank (PPR)* features. The PPR matrix is defined in closed form as:

$$\text{PPR} = p_r (\mathbf{I} - (1 - p_r) \mathbf{T})^{-1}, \quad (37)$$

where  $p_r$  denotes the restart probability.

## C Sampling Optimization in DIRECTO

The decoupling of training and sampling in discrete flow matching enables principled, training-free modifications to the sampling procedure, offering a flexible design space to enhance generation quality across digraph distributions [55]. In this section, we detail the three core parameters that govern sampling behavior: (i) time distortion functions, (ii) target guidance intensity, and (iii) stochasticity strength. Each plays a distinct role in shaping the denoising trajectory and contributes to different aspects of generation quality and structural fidelity.

**Time Distortion Functions** A central part for sampling optimization lies in the application of *time distortion functions*. These functions transform the time variable  $t \in [0, 1]$  through a bijective, monotonic mapping  $f(t)$ , yielding a distorted time variable  $t' = f(t)$ . While used in both training and sampling, their objectives differ. In training, time distortions skew the sampling distribution over time, concentrating the model’s learning capacity on specific denoising intervals. In sampling, they induce variable step sizes along the denoising trajectory, with finer resolution where structural sensitivity is highest (e.g., late-stage edits near  $t = 1$ ).

Formally, the probability density function (PDF) of the transformed time variable  $t'$  is:

$$\phi_{t'}(t') = \phi_t(t) \left| \frac{d}{dt'} f^{-1}(t') \right|, \quad \text{where } \phi_t(t) = 1 \text{ for } t \in [0, 1]. \quad (38)$$

We consider the same five representative time distortion functions from [55] that yield diverse distributions for  $t'$ :

- **Identity:**  $f(t) = t$  — Uniform time density, baseline behavior.
- **Polydec:**  $f(t) = 2t - t^2$  — Increasing density over time, emphasizing late-stage denoising.
- **Cos:**  $f(t) = \frac{1 - \cos(\pi t)}{2}$  — Concentrates density at both boundaries.
- **Revcos:**  $f(t) = 2t - \frac{1 - \cos(\pi t)}{2}$  — Peaks at intermediate times.
- **Polyinc:**  $f(t) = t^2$  — Decreasing density over time, emphasizes early steps.

In the sampling phase, the induced variable step sizes, particularly from functions like *polydec*, allow for finer resolution near the clean data, where structural coherence is most fragile. Empirically, these functions are selected based on dataset-specific properties to improve fidelity and structural constraints without need for retraining.

**Target Guidance** Another axis for improving sampling efficiency is the modification of the *conditional rate matrix*  $R_t$  to better guide the generation trajectory toward the clean target graph  $z_1$ . This is achieved by incorporating an additive guidance term:

$$R_t(z_t, z_{t+\Delta t} \mid z_1) = R_t^*(z_t, z_{t+\Delta t} \mid z_1) + \omega \cdot \frac{\delta(z_{t+\Delta t}, z_1)}{\mathcal{Z}_t^{>0} \cdot p_{t|1}(z_t \mid z_1)}. \quad (39)$$

Here,  $\omega \in \mathbb{R}_+$  controls the strength of the guidance,  $\mathcal{Z}_t^{>0}$  is a discrete variable with  $Z$  possible positive values, and  $\delta(\cdot, \cdot)$  is the Kronecker delta. Intuitively, this formulation prioritizes transitions that directly align with the clean graph.

**Stochasticity Control** The final sampling-time parameter is the *stochasticity coefficient*  $\eta$ . This parameter scales an auxiliary rate matrix  $R_t^{\text{DB}}$  that satisfies the detailed balance condition [9] and adds it to the optimal rate matrix  $R_t^*$ :

$$R_t^\eta = R_t^* + \eta \cdot R_t^{\text{DB}}. \quad (40)$$

The role of  $\eta$  is to regulate trajectory stochasticity: higher values promote broader exploration during denoising, potentially correcting suboptimal states. Setting  $\eta = 0$  recovers the deterministic path prescribed by  $R_t^*$ , minimizing the expected number of transitions.

**Sampling Optimization** Together, these sampling parameters constitute a flexible, principled toolkit for tailoring the sampling procedure to diverse graph domains and structural requirements. In our case, we optimize these parameters at sampling time to improve the performance of DIRECTO. In particular, we individually optimize each of them, and perform the final sampling using the best performing parameters in terms of V.U.N. and ratio performance. A study of the effect of these parameters on sampling performance can be found in H.5.

## D DIRECTO Training and Sampling Algorithms

This appendix provides detailed pseudocode for the training and sampling procedures used in the DIRECTO framework. Alg. 1 outlines the training loop, where a digraph is progressively noised and a denoising model is optimized to reconstruct the original graph.

We consider the original data distribution  $\mathbf{p}_1$  as well as the time distribution  $\mathcal{T}$  which in our case is set to be the uniform distribution. In addition,  $f^\theta$  refers to the denoising network, in our case the graph transformer with dual attention.

---

### Algorithm 1 DIRECTO Training

---

```

1: Input: Graph dataset  $\{G^1, \dots, G^M\} \sim \mathbf{p}_1$ 
2: while  $f_\theta$  not converged do
3:   Sample  $G \sim \mathbf{p}_1$ 
4:   Sample  $t \sim \mathcal{T}$ 
5:   Iteratively sample  $G_t \sim \mathbf{p}_{t|1}(G_t|G)$  ▷ Noising process
6:    $h \leftarrow \text{PosEnc}(G_t)$  ▷ Positional encoding
7:    $\mathbf{p}_{1|t}^\theta(\cdot|G_t) \leftarrow f_\theta(G_t, h, t)$  ▷ Denoising prediction with dual attention
8:    $\text{loss} \leftarrow \text{CE}_\lambda(G, \mathbf{p}_{1|t}^\theta(\cdot|G_t))$ 
9: end while

```

---

Alg. 2 describes the generative sampling process in which new digraphs are synthesized by iteratively denoising from an initial random digraph structure. Again, we consider  $\mathbf{p}_0 = \mathbf{p}_{noise}$  the predefined noise distribution,  $f^\theta$  the denoising graph transformer with dual attention,  $\mathbf{p}_{1|t}^\theta$  the denoising predictions, and  $\mathbf{p}_{t+\Delta t|t}^\theta$  as the update rule, see Eq. (44).

---

### Algorithm 2 DIRECTO Sampling

---

```

1: Input: # graphs to sample  $S$ 
2: for  $i = 1$  to  $S$  do
3:   Sample  $N$  from train set ▷ # nodes
4:   Sample  $G_0 \sim \mathbf{p}_0(G_0)$ 
5:   for  $t = 0$  to  $1 - \Delta t$  with step  $\Delta t$  do
6:      $h \leftarrow \text{PosEnc}(G_t)$  ▷ Positional encoding
7:      $\mathbf{p}_{1|t}^\theta(\cdot|G_t) \leftarrow f_\theta(G_t, h, t)$  ▷ Denoising prediction with dual attention
8:      $G_{t+\Delta t} \sim \mathbf{p}_{t+\Delta t|t}^\theta(G_{t+\Delta t}|G_t)$  ▷ Update rule
9:   end for
10:  Store  $G_1$  as  $G^i$ 
11: end for

```

---

## E Dataset descriptions

In this section, we provide further detailed information about the datasets described in Section 4 and used for the experiments in Section 5.

## E.1 Synthetic datasets

We outline the mathematical formulation of each graph generation strategy used in our experiments. All graphs are generated as adjacency matrices  $\mathbf{A} \in \{0, 1\}^{n \times n}$  (where  $A_{ij} = 1$  denotes a directed edge from node  $i$  to node  $j$ ), and preprocessed to adapt to the structure required by the model.

For all datasets, we generate a total of 200 graphs, split as: 128 train, 32 validation, 40 test. A study on the effect of the dataset size on the quality of the generations can be found in Appendix H.4. Furthermore, the dataset statistics can be found in Table 3.

Table 3: Synthetic dataset statistics.

Dataset	Min. nodes	Max. nodes	Avg. nodes	Min. edges	Max. edges	Avg. edges	#Train	#Val	#Test
Erdos-Renyi (ER)	20	80	46	223	3670	1446	128	32	40
SBM	44	175	106	340	3008	1426	128	32	40
ER (DAG)	20	80	49	103	1892	762	128	32	40
Price (DAG)	64	64	64	132	246	197	128	32	40

**Erdős-Renyi [19]** We generate graphs with a variable number of nodes between  $n = 20$  and  $n = 80$ . For a number of nodes  $n$ , edges are sampled independently with a fixed probability  $p = 0.6$ . The adjacency matrix  $\mathbf{A}$  is generated by:

$$A_{ij} \sim \text{Bernoulli}(p), \quad \forall i \neq j$$

To generate a second dataset of DAGs, we enforce a lower-triangular structure (i.e., edges only from higher-indexed to lower-indexed nodes), which results in graphs generated with a probability  $p = 0.3$ .

**Price’s model [15]** This is the directed version of the Barabási-Albert or preferential attachment model, which simulates the growth of citation networks. We build DAGs sequentially for a fixed number of nodes  $N = 64$ . Each new node  $i$  forms  $m = \log_2(N)$  edges to existing nodes  $j$  with probability proportional to their degree:

$$\mathbb{P}(i \rightarrow j) \propto \text{deg}(j).$$

Since the number of nodes is fixed to  $N = 64$ , mean out-degree results in  $m = 6$ . In practice, we implement this "bag" of nodes that replicates existing connections. For each new node  $i$ , we sample  $m$  destination nodes from the bag. Then, for each selected node  $j$ , we set  $A_{ij} = 1$  and add  $i$  and the selected nodes to the bag. This ensures a directed acyclic graph (DAG) due to the order of node addition.

**Stochastic Block Model [26]** We create  $K$  communities with sizes  $\{n_1, n_2, \dots, n_K\}$ . We set the number of communities between  $K = 2$  and  $K = 5$ , and the number of nodes per community between 20 and 40. The probability of an edge between any two nodes depends on their community assignments

$$A_{ij} \sim \text{Bernoulli}(P_{z_i z_j})$$

where  $z_i \in \{1, \dots, K\}$  is the block assignment of node  $i$  and  $P \in [0, 1]^{K \times K}$  is a matrix of intra- and inter-community connection probabilities. In particular, we use

$$P_{kk} = p_{\text{intra}} = 0.3, \quad P_{kl} = p_{\text{inter}} = 0.05 \text{ for } k \neq l$$

to generate a block-structured, directed graph.

## E.2 TPU Tiles

In this dataset introduced in [54], each DAG represents a computation within a machine learning workload, such as a training epoch or an inference step. Each of the 12602 data points includes a computational graph, a specific compilation configuration, and the execution time of the graph when compiled with that configuration. The dataset features different model architectures, such as ResNets, EfficientNets, Masked R-CNNs, and Transformers, with graphs of up to  $\sim 400$  nodes.

We adopt the processing and splits from [39]. Details on dataset statistics for the three different splits can be found in Table 4.

Table 4: TPU Tiles dataset statistics.

Dataset	Min. nodes	Max. nodes	Avg. nodes	Min. edges	Max. edges	Avg. edges	# Graphs
Train	2	394	41	1	711	43	5040
Validation	2	113	41	1	123	43	630
Test	2	154	41	1	249	44	631

### E.3 Visual Genome

The Visual Genome dataset [35] aims at bridging computer vision and natural language understanding by providing richly annotated images. It comprises over 100,000 images annotated with object labels, attributes, relationships, which allows to capture the presence of objects but also their attributes and interactions. It has become a standard benchmark for tasks such as scene graph generation, visual question answering, and grounded language understanding.

To build the directed graph dataset, we set 3 types of nodes: objects, attributes, and relationships, with the actual node class being the text label. Then, we link them via directed edges according to the visual rules provided in the original data and taking into account that:

1. **Objects** have outgoing edges to attributes and relationships and incoming edges from relationships.
2. **Relationships** have outgoing edges to objects and incoming edges from objects.
3. **Attributes** have no outgoing edges and incoming edges from objects.

Once we built the digraphs, we select a relevant subset from this raw dataset by keeping graphs with 20 to 40 nodes, and with a minimum of 25 edges per graph. Then, for each graph, we only consider objects, attributes, and relationships that are in the top-20 in terms of prevalence in the full dataset, ending with 60 node classes. We randomly split the graphs into 203 train, 52 validation and 63 test graphs, with detailed statistics of each split available in Table 5. The total number of cyclic graph in the dataset is 119 ( $\sim 37.5\%$  of the digraphs).

Table 5: Visual Genome dataset statistics.

Dataset	Min. nodes	Max. nodes	Avg. nodes	Min. edges	Max. edges	Avg. edges	# Graphs
Global	21	40	34	25	47	28	317
Train	21	40	33	25	47	28	203
Validation	24	40	34	25	40	28	51
Test	21	40	34	25	36	28	63

The selected top-20 objects, relationships, and attributes are:

- **Objects:** ['window', 'tree', 'man', 'shirt', 'wall', 'person', 'building', 'ground', 'sign', 'light', 'sky', 'head', 'leaf', 'leg', 'hand', 'pole', 'grass', 'hair', 'car', 'cloud']
- **Relationships:** ['on', 'has', 'in', 'of', 'wearing', 'with', 'behind', 'holding', 'on top of', 'on a', 'near', 'next to', 'has a', 'on', 'under', 'by', 'of a', 'wears', 'above', 'sitting on']
- **Attributes:** ['white', 'black', 'blue', 'green', 'red', 'brown', 'yellow', 'small', 'large', 'wooden', 'gray', 'silver', 'metal', 'orange', 'grey', 'tall', 'long', 'dark', 'pink', 'clear']

## F Further details on evaluation metrics

In this section, we detail the statistical procedures used to evaluate the graphs generated by our model. We detail how we compute the validity metrics for the different datasets, as well as how we make the validity and uniqueness computation more efficient.

## F.1 Validity metrics

**Erdős-Renyi** Given a graph  $G = (V, E)$  with  $n = |V|$  nodes and  $m = |E|$  edges, we want to determine whether the graph likely originates from an Erdős-Rényi model  $G(n, p)$  with edge probability  $p$  using a Wald test [24]. For that, we follow the following steps distinguishing the cases in which the graphs are DAGs or not:

1. **Empirical edge probability:** we compute the number of possible edges

$$m_{\max} = \begin{cases} \frac{n(n-1)}{2} & \text{if the graph acyclic} \\ n(n-1) & \text{if the graph is not acyclic} \end{cases}$$

and then estimate the empirical probability of edge presence  $\hat{p} = \frac{m}{m_{\max}}$ .

2. **Wald test statistic:** the Wald statistic tests the null hypothesis  $H_0 : \hat{p} = p$ , where  $p$  is the expected edge probability:

$$W = \frac{(\hat{p} - p)^2}{\hat{p}(1 - \hat{p}) + \varepsilon}$$

and where we add a small regularization  $\varepsilon = 10^{-6}$  to prevent division by zero.

3.  **$p$ -value computation:** assuming the null hypothesis, the Wald statistic  $W$  asymptotically follows a Chi-squared distribution with 1 degree of freedom:

$$p\text{-value} = 1 - F_{\chi^2}(W; df = 1)$$

where  $F_{\chi^2}$  is the cumulative distribution function (CDF) of the Chi-squared distribution.

In the rare limit case where graphs contain only one node, we consider that the graph does not follow the distribution.

**Stochastic Block Model** To assess whether a graph  $G = (V, E)$  conforms to a Stochastic Block Model (SBM), we recover the block structure and probability parameters. The test then computes Wald statistics for intra- and inter-block edge probabilities.

1. **Block assignment via model inference:** Given the adjacency matrix  $A \in \{0, 1\}^{n \times n}$  of a graph  $G$ , we use an algorithm [52] to infer the stochastic block model (block assignment) from a given network:

$$\text{Infer } z : V \rightarrow \{1, \dots, B\} \quad \text{using } \min \mathcal{L}(G, z)$$

where  $B$  is the number of non-empty blocks found and  $\mathcal{L}$  is the description length. The model can be further refined using Markov-Chain Monte Carlo (MCMC) for  $T$  timesteps.

2. **Estimating intra- and inter-block probabilities:** let  $N_i$  be number of nodes in block  $i$  and  $E_{ij}$  the number of edges between block  $i$  and block  $j$  recovered by the algorithm in the previous step. Then the estimated probabilities for directed SBM graphs are:

$$\hat{p}_{\text{intra},i} = \frac{E_{ii}}{N_i(N_i - 1) + \varepsilon}$$

$$\hat{p}_{\text{inter},ij} = \frac{E_{ij}}{N_i N_j + \varepsilon}, \quad i \neq j$$

where  $\varepsilon = 10^{-6}$  is a small regularization constant.

3. **Wald test statistic:** we compare the empirical estimates to expected values  $p_{\text{intra}}$  and  $p_{\text{inter}}$  using a Wald statistic:

$$W_{ii} = \frac{(\hat{p}_{\text{intra},i} - p_{\text{intra}})^2}{\hat{p}_{\text{intra},i}(1 - \hat{p}_{\text{intra},i}) + \varepsilon}$$

$$W_{ij} = \frac{(\hat{p}_{\text{inter},ij} - p_{\text{inter}})^2}{\hat{p}_{\text{inter},ij}(1 - \hat{p}_{\text{inter},ij}) + \varepsilon}, \quad i \neq j$$

4. ***p*-value computation:** assuming the null hypothesis (i.e., estimated probabilities match expected ones), each Wald statistic follows a Chi-squared distribution with 1 degree of freedom:

$$p_{ij} = 1 - F_{\chi^2}(W_{ij}; df = 1),$$

and therefore the overall *p*-value can be computed as the mean of all  $p_{ij}$

$$p\text{-value} = \frac{1}{B^2} \sum_{i=1}^B \sum_{j=1}^B p_{ij}$$

**Price’s model** To assess whether a graph follows a Price’s model, we use a nonparametric two-sample Kolmogorov–Smirnov (KS) test:

1. **Computing degree distribution:** let  $D = \{d_1, d_2, \dots, d_n\}$  be the degree sequence of the nodes in  $G$ . To reduce noise and ensure a more stable distribution, ignore nodes with degree  $\leq 1$  and end with the distribution  $D' = \{d_i \in D \mid d_i > 1\}$ .
2. **Synthetic graph generation:** we construct a synthetic graph  $G_{BA}$  using the Barabási–Albert model with the same number of nodes:  $G_{BA} \sim BA(n, m)$ , where  $n = |V|$  is the number of nodes and  $m = 6$  is the number of edges each new node adds during attachment, fixed to the same value as in our data generation. The degree sequence of the synthetic graph is  $D_{BA}$ .
3. **Kolmogorov-Smirnov Two-Sample test:** we perform a two-sample Kolmogorov–Smirnov (KS) test to compare the empirical distribution functions of  $D'$  and  $D_{BA}$

$$p\text{-value} = 1 - \text{KS}_2 \text{ sampled}(D', D_{BA})$$

which evaluates the null hypothesis:  $H_0 : D' \sim D_{BA}$ .

**TPU Tiles** For the TPU Tiles dataset, we report the percentage of valid Directed Acyclic Graphs (DAGs) as our primary validity metric, reflecting our focus on accurately reconstructing acyclic computational graphs.

**Visual Genome** As seen in Appendix E.3, by construction, object nodes can have outgoing edges to relationship or attribute nodes but only receive incoming edges from relationship nodes. Relationship nodes only have incoming edges from object nodes and send outgoing edges to objects. Finally, attributes can only receive edges from object nodes and do not have any outgoing edges. Therefore, to measure digraph validity we evaluate that the generated graphs verify these constraints.

## F.2 Uniqueness and novelty

To evaluate the quality and novelty of generated graphs, we employ the usual metrics based on graph isomorphism. In particular we measure the fraction of isomorphic graphs from the sampled set to the train set (uniqueness) and the fraction of graphs from the sampled set that are not isomorphic to any other in the same sampled set (novelty).

However, since exact graph isomorphism testing can be computationally expensive, particularly for large or dense graphs such as the one in the TPU Tiles dataset, we incorporate a timeout mechanism. Specifically, if an isomorphism check does not complete within 5 seconds, it is treated as a timeout and the graph is conservatively assumed to be non-isomorphic.

In Table 2, we see that in three of the model configurations the computations timed out. We report the average percentage of graphs that could not be tested, which was 2.5% for DIGRESS, 0.8% for DEF0G, and 2% for DIRECTO RRWP.

## F.3 Maximum Mean Discrepancy metrics

For the different metrics, we adapt previous work from [46, 36]. We propose to measure both out-degree and in-degree distributions, as well as clustering, spectre and wavellet. To measure the *clustering* coefficient, we compute the distribution of directed local clustering coefficients using `networkx` function `clustering()`, which supports digraphs. For the spectral features (*spectre* and *wavellet*), we derive the spectral features from the directed Laplacian, as described in Section 4.

In addition, the *orbit* metric that was also computed in [46] has not been adapted to the directed setting as it relies on the Orbit Counting Algorithm (ORCA) which counts graphlets in networks but is only implemented in the undirected setting. Therefore, adapting this metric to the directed setting remains an open challenge.

## G Experimental details

### G.1 Details on baselines

**Maximum Likelihood Estimation (MLE)** We define a simple baseline by estimating empirical probabilities from the training dataset via maximum likelihood estimation. The following distributions are computed:

1. **Number of Nodes Distribution:** Let  $n$  denote the number of nodes in a graph. The empirical distribution over  $n$  is given by:

$$P(n) = \frac{\text{Number of training graphs with } n \text{ nodes}}{\text{Total number of training graphs}}.$$

2. **Node Class Distribution:** Let  $c$  be a node class. The empirical node class distribution is:

$$P(v = c) = \frac{\text{Number of nodes of class } c}{\text{Total number of nodes in all training graphs}}.$$

3. **Edge Type Distribution Conditioned on Node Pairs:** Let  $(v_i, v_j)$  be a pair of nodes such that  $v_i$  has class  $c_a$  and  $v_j$  has class  $c_b$ . Let  $e_{ij} \in \{1, \dots, K\}$  denote the edge type between them (with  $K$  total edge types). The empirical conditional distribution is:

$$P(e_{ij} = k \mid v_i = c_a, v_j = c_b) = \frac{\text{Number of edges of type } k \text{ between } (c_a, c_b)}{\sum_{k'=1}^K \text{Number of edges of type } k' \text{ between } (c_a, c_b)}.$$

These distributions are stored and later used to construct graphs by first sampling the number of nodes, then sampling node types independently, and finally sampling edge types between each node pair according to the conditional edge distribution.

**D-VAE [77]** This autoregressive method encodes and decodes directed acyclic graphs (DAGs) using an asynchronous message passing scheme. Unlike standard graph neural networks (GNNs), which apply simultaneous message passing across all nodes and updates them all at once, D-VAE updates nodes sequentially, allowing it to capture the computational flow within the graph rather than just its structure. During generation, the DAG is built one node at a time in topological order, with edges always directed toward newly added nodes ensuring the resulting graph remains acyclic. To enable this process, input graphs must be topologically sorted before being processed by the model.

To reproduce this baseline, we adapted the code available in their [GitHub](#) and arranged both the TPU Tiles and ER-DAG datasets to match the input format expected by the original model. We used the same hyperparameter configurations as suggested in the original paper to ensure consistency in training, which happened for 500 epochs. After generation, we converted the output DAGs back into the required format for compatibility with our evaluation metrics.

For ER-DAG, we tested two different learning rates  $10^{-4}$  and  $10^{-5}$ , and ended using the model with  $10^{-5}$ , which resulted in better V.U.N. results with a training time of  $\sim 3$ min per epoch. For TPU Tiles, due to the large size of the dataset and some of the graphs in it, it was impossible to perform a training epoch in a reasonable time, as each of them was predicted to take  $\sim 12$ h.

**LayerDAG [39]** This autoregressive diffusion model generates DAGs by converting them into sequences of bipartite graphs, effectively enabling a layer-wise tokenization suitable for autoregressive generation. At each step, a layer-wise diffusion process captures dependencies between nodes that are not directly comparable (i.e., not connected by a path). As with other autoregressive DAG models, the input graphs must be topologically sorted to ensure correct processing.

To reproduce this baseline, we adopted the implementation from [GitHub](#) adapted the ER-DAG data to the correct format ordering the graphs topologically, as TPU Tiles was already in the correct format.

We kept the hyperparameters from the default configurations, including the number of epochs for each of the elements of the model. After generation, we converted the output DAGs back into the required format for compatibility with our evaluation metrics.

**DiGress [67]** To benchmark against DIGRESS, we consider its directed version by simply removing the symmetrization operations. This corresponds to DIRECTO-DD without dual attention and using the Laplacian positional encoding.

**DeFoG [55]** To benchmark against DEFoG, we consider its directed version by again removing the symmetrization operations. In this case this corresponds to DIRECTO without dual attention and using the RRWP Positional encoding (without PPR).

## G.2 Training setup

This section details the training hyperparameters used across all experiments presented in the main text. Unless otherwise specified, the values reported below were used uniformly across all positional encoding variants and ablation settings. In particular, we report the choices for the training, for the positional encodings employed, and for the sampling.

**Training** The training hyperparameters used in our experiments are summarized in Table 6. These settings were consistently applied across all training runs for both DIRECTO and DIRECTO-DD (with discrete diffusion). We trained each model for up to 10,000 epochs, stopping the runs based on validation performance to account for variations in convergence behavior across datasets.

Table 6: Training and model hyperparameters used in all experiments.

Hyperparameter	Value
Training Settings	
Learning rate	0.0002
Weight decay	$1 \times 10^{-12}$
Optimizer	AdamW
Model Settings	
Initial distribution	Marginal
Train distortion	Identity
Number of diffusion steps	500
Noise schedule	Cosine
Number of layers	5
Hidden MLP dimensions	$X: 256, E: 128, y: 128$
Transformer hidden dimensions	$d_x: 256, d_e: 64, d_y: 64, n_{head}: 8$
Feedforward dims	$\dim_{ffx}: 256, \dim_{ffe}: 128, \dim_{ffy}: 128$
Training loss weights ( $\lambda_{train}$ )	[5, 0]

**Positional encodings** For RRWP, we set the walk length parameter to  $K = 20$ . For MagLap with  $Q = 5$ , we used equidistant potentials  $\mathbf{q}_5 = (0, 0.1, 0.2, 0.3, 0.4)$ . For  $Q = 10$ , we selected again 10 equidistant potentials  $\mathbf{q}_{10} = (0.01, \dots, 0.1)$ . In all cases, we then kept the  $k = 10$  first eigenvalues and eigenvectors (padding with null values whenever the graphs had less than 10 nodes).

**Sampling** To perform sampling optimization, we conducted a targeted search over the three key hyperparameters: the time distortion function, the target guidance factor ( $\omega$ ), and the stochasticity coefficient ( $\eta$ ). Each hyperparameter was varied independently, while the others were held at their default values (identity distortion and  $\omega = \eta = 0$ ). For computational efficiency, all searches were performed using 100 sampling steps, and each configuration was evaluated using five independent sampling runs to ensure robustness. An exception was made for the TPU Tiles dataset, where only a single sampling run was performed per configuration due to the large size of the dataset and some individual graphs.

Based on the outcome of this optimization, we selected the best-performing configurations for each combination of dataset and positional encoding, balancing the trade-off between V.U.N and ratio. The optimal configurations of the results reported in the main paper are summarized in Table 7. For

the final evaluation, we performed five sampling runs per configuration using 1000 sampling steps. In all cases, the number of generated graphs matched the size of the test set (40 for synthetic datasets, 63 for Visual Genome), except for TPU Tiles, where we again limited the number of sampled digraphs to 40 due to computational constraints.

For DIRECTO-DD we performed 500 sampling steps in all the different model configurations.

Table 7: Optimal sampling hyperparameters for each dataset and positional encoding variant.

Encoding	Distortion	$\omega$	$\eta$
ER-DAG			
Baseline	Polydec	2	10
RRWP	Polydec	0.1	25
MagLap	Polydec	0	100
SBM			
Baseline	Revcos	0.3	5
RRWP	Polyinc	0.01	10
MagLap	Polydec	0.01	10
TPU Tiles			
Baseline	Polydec	0.01	25
RRWP	Polyinc	0.3	10
MagLap	Polydec	0.4	50
Visual Genome			
Baseline	Cos	0.05	0
RRWP	Polydec	0.3	100
MagLap	Polydec	0.1	10

### G.3 Resources and runtime

All experiments were conducted on a single NVIDIA A100-SXM4-80GB GPU. Table 8 summarizes the runtime of the training and sampling stages across the different datasets. These timings reflect the training time until best performance and the average sampling time per sample, for all the configurations reported in the main results for DIRECTO.

Table 8: Training and sampling runtimes for each dataset and positional encoding variant.

Encoding	Training graphs	Training time (h)	Graphs sampled	Sampling time (min/sample)
ER-DAG				
Baseline	120	13.6	40	0.125
RRWP	120	13.5	40	0.3
MagLap	120	14.4	40	0.8
SBM				
Baseline	120	23.7	40	0.3
RRWP	120	13.7	40	0.5
MagLap	120	21	40	2.1
TPU Tiles				
Baseline	5040	10	40	1.1
RRWP	5040	21	40	1.1
MagLap	5040	49	40	6.7
Visual Genome				
Baseline	203	7.5	63	0.9
RRWP	203	9	63	1.1
MagLap	203	10	63	1.3

## H Additional results

In this section, we present additional results that offer deeper insights into our model’s performance and design choices. Specifically, we analyze the impact of the dual attention mechanism and the

choice of positional encoding, compare performance on ER and DAG accuracy metrics, examine how dataset size influences generation quality, and evaluate the effect of the sampling optimization step in discrete flow matching.

### H.1 The role of dual attention

To assess the impact of the dual-attention mechanism in our model, we conduct an ablation study in which we remove the cross-attention between edge features and their transposes. This mechanism is designed to capture both source-to-target and target-to-source interactions, which are critical for modeling directional dependencies in directed graphs. By disabling dual attention, we isolate its contribution to generation quality, particularly in terms of validity, expressiveness, and generalization. We compare the full model with its ablated variant across model combinations to quantify the importance of this component.

**DIRECTO** Table 9 presents ablation results highlighting the impact of the dual attention mechanism in our method. The results are presented for two datasets: ER-DAG and SBM.

Table 9: Directed Graph Generation performance across different transformer architectures using discrete flow matching.

Dataset	Model	Out-degree ↓	In-degree ↓	Clustering ↓	Spectre ↓	Wavelet ↓	Ratio ↓	Valid ↑	Unique ↑	Novel ↑	V.UN. ↑
ER-DAG	No PE	0.0078 ± 0.0008	0.0078 ± 0.0010	0.1293 ± 0.0024	0.0735 ± 0.0023	0.0874 ± 0.0030	12.2 ± 0.4	0 ± 0.0	100 ± 0.0	100 ± 0.0	0 ± 0.0
	No PE - Dual	0.0109 ± 0.0012	0.0110 ± 0.0012	0.0807 ± 0.0147	0.0073 ± 0.0007	0.0215 ± 0.0017	3.0 ± 0.2	47 ± 12.1	100 ± 0.0	100 ± 0.0	47 ± 12.1
	RRWP	0.0109 ± 0.0019	0.0108 ± 0.0017	0.0540 ± 0.0112	0.0061 ± 0.0008	0.0030 ± 0.0005	1.3 ± 0.1	67.5 ± 1.6	100 ± 0.0	100 ± 0.0	67.5 ± 1.6
	RRWP - Dual	0.0107 ± 0.0019	0.0104 ± 0.0012	0.1209 ± 0.0194	0.0054 ± 0.0005	0.0043 ± 0.0008	1.7 ± 0.1	94 ± 1.0	100 ± 0.0	100 ± 0.0	94 ± 1.0
	MagLap	0.0113 ± 0.0024	0.0110 ± 0.0015	0.1196 ± 0.0107	0.0061 ± 0.0011	0.0029 ± 0.0006	1.7 ± 0.2	74 ± 4.4	100 ± 0.0	100 ± 0.0	74 ± 4.4
	MagLap - Dual	0.0110 ± 0.0017	0.0116 ± 0.0021	0.0509 ± 0.0017	0.0062 ± 0.0014	0.0027 ± 0.0005	1.3 ± 0.2	91 ± 2.5	100 ± 0.0	100 ± 0.0	91 ± 2.5
SBM	No PE	0.0038 ± 0.0021	0.0040 ± 0.0020	0.1912 ± 0.0178	0.0975 ± 0.0028	0.0961 ± 0.0071	20.5 ± 2.0	0 ± 0.0	100 ± 0.0	100 ± 0.0	0 ± 0.0
	No PE - Dual	0.0038 ± 0.0011	0.0037 ± 0.0010	0.0638 ± 0.0059	0.0037 ± 0.0003	0.0127 ± 0.0018	3.5 ± 0.4	48.5 ± 6.4	100 ± 0.0	100 ± 0.0	48.5 ± 6.4
	RRWP	0.0036 ± 0.0009	0.0034 ± 0.0008	0.1276 ± 0.0065	0.0345 ± 0.0028	0.0961 ± 0.0071	21.4 ± 1.6	13.5 ± 5.4	100 ± 0.0	100 ± 0.0	13.5 ± 5.4
	RRWP - Dual	0.0038 ± 0.0011	0.0037 ± 0.0012	0.0492 ± 0.0041	0.0035 ± 0.0007	0.0015 ± 0.0004	1.4 ± 0.2	87 ± 5.1	100 ± 0.0	100 ± 0.0	87 ± 5.1
	MagLap	0.0033 ± 0.0008	0.0034 ± 0.0008	0.1356 ± 0.0118	0.0481 ± 0.0022	0.1250 ± 0.0017	27.7 ± 4.3	21.5 ± 2.0	100 ± 0.0	100 ± 0.0	21.5 ± 2.0
	MagLap - Dual	0.0039 ± 0.0011	0.0036 ± 0.0010	0.0653 ± 0.0026	0.0033 ± 0.0003	0.0038 ± 0.0010	1.9 ± 0.3	77 ± 7.6	100 ± 0.0	100 ± 0.0	77 ± 7.6

In particular, we observe that, across both datasets, the inclusion of the dual attention mechanism consistently improves the validity of the generated graphs and reduces structural discrepancies as measured by clustering, spectral, and wavelet distances. In the ER-DAG setting, models with dual attention (e.g., RRWP-Dual and MagLap-Dual) significantly outperform their non-dual counterparts in validity—achieving up to 94% validity with RRWP-Dual and 91% with MagLap-Dual, compared to just 67.5% and 74%, respectively. These models also demonstrate better structural fidelity, particularly in clustering and spectral metrics. A similar trend is observed in the SBM dataset, where dual attention boosts validity (e.g., RRWP-Dual: 87%, MagLap-Dual: 77%). These results demonstrate how incorporating bidirectional information flow into the attention mechanism contributes to improved model performance and provides insight into the effectiveness of this architectural component.

**DIRECTO-DD** Table 10 shows a second ablation assessing the contribution of the dual attention mechanism within the discrete diffusion framework. In this case, we see a similar pattern to that observed under discrete flow matching: the incorporation of dual attention leads to consistent gains in graph validity across both ER-DAG and SBM datasets. Models augmented with dual attention not only produce more valid graphs but also exhibit improved alignment with structural statistics such as clustering, spectre, and wavelet.

Table 10: Directed Graph Generation performance across different transformer architectures using discrete diffusion.

Dataset	Model	Out-degree ↓	In-degree ↓	Clustering ↓	Spectre ↓	Wavelet ↓	Ratio ↓	Valid ↑	Unique ↑	Novel ↑	V.UN. ↑
ER-DAG	No PE	0.0094 ± 0.0024	0.0095 ± 0.0023	0.1221 ± 0.0122	0.0814 ± 0.0030	0.1094 ± 0.0066	14.4 ± 0.8	0 ± 0.0	100 ± 0.0	100 ± 0.0	0 ± 0.0
	No PE - Dual	0.0149 ± 0.0037	0.0138 ± 0.0035	0.1256 ± 0.0088	0.0089 ± 0.0018	0.0106 ± 0.0014	2.6 ± 0.3	53 ± 2.9	100 ± 0.0	100 ± 0.0	53 ± 2.9
	RRWP	0.0147 ± 0.0038	0.0139 ± 0.0038	0.0985 ± 0.0154	0.0067 ± 0.0009	0.0038 ± 0.0009	2.1 ± 0.3	42 ± 1.0	100 ± 0.0	100 ± 0.0	42 ± 1.0
	RRWP - Dual	0.0142 ± 0.0040	0.0129 ± 0.0034	0.0408 ± 0.0053	0.0055 ± 0.0010	0.0048 ± 0.0014	1.4 ± 0.3	79 ± 3.7	100 ± 0.0	100 ± 0.0	79 ± 3.7
	MagLap	0.0144 ± 0.0040	0.0135 ± 0.0038	0.0792 ± 0.0126	0.0071 ± 0.0012	0.0036 ± 0.0011	1.6 ± 0.3	59 ± 6.8	100 ± 0.0	100 ± 0.0	59 ± 6.8
	MagLap - Dual	0.0142 ± 0.0044	0.0135 ± 0.0034	0.0438 ± 0.0071	0.0057 ± 0.0013	0.0046 ± 0.0010	1.4 ± 0.3	69 ± 6.4	100 ± 0.0	100 ± 0.0	69 ± 6.4
SBM	No PE	0.0038 ± 0.0021	0.0040 ± 0.0020	0.1912 ± 0.0177	0.0120 ± 0.0019	0.0975 ± 0.0081	20.5 ± 2.0	0 ± 0.0	100 ± 0.0	100 ± 0.0	0 ± 0.0
	No PE - Dual	0.0037 ± 0.0020	0.0039 ± 0.0019	0.0721 ± 0.0059	0.0055 ± 0.0007	0.0403 ± 0.0067	8.8 ± 1.3	35 ± 9.1	100 ± 0.0	100 ± 0.0	35 ± 9.1
	RRWP	0.0038 ± 0.0019	0.0038 ± 0.0018	0.1085 ± 0.0205	0.0088 ± 0.0009	0.0359 ± 0.0043	8.5 ± 0.3	4 ± 2.0	100 ± 0.0	100 ± 0.0	4 ± 2.0
	RRWP - Dual	0.0036 ± 0.0019	0.0036 ± 0.0018	0.0592 ± 0.0027	0.0038 ± 0.0007	0.0027 ± 0.0009	1.7 ± 0.4	81.5 ± 3.2	100 ± 0.0	100 ± 0.0	81.5 ± 3.2
	MagLap	0.0038 ± 0.0019	0.0039 ± 0.0019	0.0186 ± 0.0046	0.0043 ± 0.0006	0.0543 ± 0.0072	11.3 ± 1.6	10 ± 4.2	100 ± 0.0	100 ± 0.0	10 ± 4.2
	MagLap - Dual	0.0035 ± 0.0018	0.0036 ± 0.0018	0.0670 ± 0.0032	0.0045 ± 0.0008	0.0033 ± 0.0013	1.9 ± 0.4	66.5 ± 4.1	100 ± 0.0	100 ± 0.0	66.5 ± 4.1

## H.2 The role of positional encodings

To evaluate the importance of positional encodings in our model, we perform an ablation study comparing different options. Directed graphs lack a canonical node ordering, making positional information crucial for capturing structural context. We test several variants, including no positional encoding, encodings that do not take into accounts directed information, and then different directed positional encodings. This analysis isolates how each encoding contributes to the model’s ability to generate valid and semantically meaningful graphs. We report performance across synthetic datasets for both discrete diffusion and flow matching.

**DIRECTO** Table 11 presents an ablation study analyzing the impact of various positional encoding (PE) strategies on directed graph generation performance under the discrete flow matching framework. This evaluation highlights the critical role of positional information in enabling models to capture the asymmetric and hierarchical structure inherent to directed graphs.

Table 11: Directed Graph Generation performance across different positional encodings using discrete Flow Matching.

Dataset	Model	Out-degree ↓	In-degree ↓	Clustering ↓	Spectre ↓	Wavelet ↓	Ratio ↓	Valid ↑	Unique ↑	Novel ↑	V.U.N. ↑
ER-DAG	No PE	0.0109 ± 0.0012	0.0110 ± 0.0012	0.0807 ± 0.0147	0.0073 ± 0.0007	0.0215 ± 0.0017	3.0 ± 0.2	47 ± 12.1	100 ± 0.0	100 ± 0.0	47 ± 12.1
	Lap	0.0119 ± 0.0020	0.0115 ± 0.0025	0.1272 ± 0.0224	0.0047 ± 0.0009	0.0048 ± 0.0005	1.8 ± 0.0	84 ± 4.9	100 ± 0.0	100 ± 0.0	84 ± 4.9
	RRWP	0.0107 ± 0.0019	0.0104 ± 0.0012	0.1209 ± 0.0194	0.0054 ± 0.0005	0.0043 ± 0.0008	1.7 ± 0.1	94 ± 1.0	100 ± 0.0	100 ± 0.0	94 ± 1.0
	MagLap	0.0110 ± 0.0017	0.0116 ± 0.0021	0.0509 ± 0.0017	0.0062 ± 0.0014	0.0027 ± 0.0005	1.3 ± 0.2	91 ± 2.5	100 ± 0.0	100 ± 0.0	91 ± 2.5
	MagLap (Q = 5)	0.0112 ± 0.0015	0.0107 ± 0.0022	0.0527 ± 0.0059	0.0056 ± 0.0009	0.0032 ± 0.0006	1.3 ± 0.2	91.5 ± 2.5	100 ± 0.0	100 ± 0.0	91.5 ± 2.5
	MagLap (Q = 10)	0.0117 ± 0.0014	0.0110 ± 0.0015	0.0711 ± 0.0120	0.0055 ± 0.0016	0.0026 ± 0.0004	1.3 ± 0.2	92 ± 3.7	100 ± 0.0	100 ± 0.0	92 ± 3.7
SBM	No PE	0.0038 ± 0.0011	0.0037 ± 0.0010	0.0638 ± 0.0059	0.0037 ± 0.0003	0.0127 ± 0.0018	3.5 ± 0.4	48.5 ± 6.4	100 ± 0.0	100 ± 0.0	48.5 ± 6.4
	Lap	0.0040 ± 0.0012	0.0038 ± 0.0011	0.0552 ± 0.0042	0.0048 ± 0.0006	0.0044 ± 0.0008	2.1 ± 0.3	71.5 ± 4.1	100 ± 0.0	100 ± 0.0	71.5 ± 4.1
	RRWP	0.0038 ± 0.0011	0.0037 ± 0.0012	0.0492 ± 0.0041	0.0035 ± 0.0007	0.0015 ± 0.0004	1.4 ± 0.2	87 ± 5.1	100 ± 0.0	100 ± 0.0	87 ± 5.1
	MagLap	0.0039 ± 0.0011	0.0036 ± 0.0010	0.0653 ± 0.0026	0.0033 ± 0.0003	0.0038 ± 0.0010	1.9 ± 0.3	77 ± 7.6	100 ± 0.0	100 ± 0.0	77 ± 7.6
	MagLap (Q = 5)	0.0039 ± 0.0010	0.0038 ± 0.0011	0.0748 ± 0.0028	0.0041 ± 0.0005	0.0070 ± 0.0015	2.6 ± 0.2	92.5 ± 2.2	100 ± 0.0	100 ± 0.0	92.5 ± 2.2
	MagLap (Q = 10)	0.0039 ± 0.0012	0.0038 ± 0.0010	0.0654 ± 0.0052	0.0038 ± 0.0003	0.0039 ± 0.0008	2.0 ± 0.3	96.5 ± 2.5	100 ± 0.0	100 ± 0.0	96.5 ± 2.5

Overall, the inclusion of any form of positional encoding significantly improves generation validity compared to the baseline with no PE. Among the methods tested, directed encodings like RRWP and magnetic Laplacian-based variants demonstrate particularly strong performance. These encodings consistently enhance graph validity and reduce MMD ratio in both datasets. Notably, the MagLap variant with multiple potentials ( $Q = 10$ ) achieves the best results in terms of validity and structural fidelity, although resulting in a higher computational cost.

Interestingly, although classical Laplacian encodings (Lap) also play a role in increasing the V.U.N. ratio, they obtain worse results than the directed counterparts, emphasizing that for directed generation tasks, the choice of positional encoding is not merely a design detail but a relevant architectural decision that affects model success.

**DIRECTO-DD** Table 12 presents an ablation study assessing the influence of various positional encodings within the discrete diffusion framework across four synthetic datasets: SBM, ER-DAG, ER, and Price’s model.

Table 12: Directed Graph Generation performance across different positional encodings using discrete diffusion.

Dataset	Model	Out-degree ↓	In-degree ↓	Clustering ↓	Spectre ↓	Wavelet ↓	Ratio ↓	Valid ↑	Unique ↑	Novel ↑	V.U.N. ↑
ER-DAG	No PE	0.0149 ± 0.0037	0.0138 ± 0.0035	0.1256 ± 0.0088	0.0089 ± 0.0018	0.0106 ± 0.0014	2.6 ± 0.3	53 ± 2.9	100 ± 0.0	100 ± 0.0	53 ± 2.9
	Lap	0.0138 ± 0.0038	0.0144 ± 0.0042	0.0462 ± 0.0071	0.0055 ± 0.0011	0.0052 ± 0.0015	1.5 ± 0.3	67 ± 5.3	100 ± 0.0	100 ± 0.0	67 ± 5.3
	RRWP	0.0142 ± 0.0040	0.0129 ± 0.0034	0.0408 ± 0.0053	0.0055 ± 0.0010	0.0048 ± 0.0014	1.4 ± 0.3	79 ± 3.7	100 ± 0.0	100 ± 0.0	79 ± 3.7
	MagLap	0.0142 ± 0.0044	0.0135 ± 0.0034	0.0438 ± 0.0071	0.0057 ± 0.0013	0.0046 ± 0.0010	1.4 ± 0.3	69 ± 6.4	100 ± 0.0	100 ± 0.0	69 ± 6.4
	MagLap (Q = 5)	0.0135 ± 0.0032	0.0140 ± 0.0045	0.0596 ± 0.0081	0.0061 ± 0.0007	0.0037 ± 0.0017	1.4 ± 0.2	78.5 ± 2.5	100 ± 0.0	100 ± 0.0	78.5 ± 2.5
	MagLap (Q = 10)	0.0145 ± 0.0040	0.0134 ± 0.0033	0.582 ± 0.0083	0.0063 ± 0.0015	0.0034 ± 0.0011	1.5 ± 0.2	85 ± 9.2	100 ± 0.0	100 ± 0.0	85 ± 9.2
SBM	No PE	0.0037 ± 0.0020	0.0039 ± 0.0019	0.0721 ± 0.0059	0.0055 ± 0.0007	0.0403 ± 0.0067	8.8 ± 1.3	35 ± 9.1	100 ± 0.0	100 ± 0.0	35 ± 9.1
	Lap	0.0037 ± 0.0020	0.0038 ± 0.0017	0.0531 ± 0.0042	0.0038 ± 0.0006	0.0106 ± 0.0009	1.4 ± 0.4	81 ± 3.7	100 ± 0.0	100 ± 0.0	81 ± 3.7
	RRWP	0.0036 ± 0.0019	0.0036 ± 0.0018	0.0592 ± 0.0027	0.0038 ± 0.0007	0.0027 ± 0.0009	1.7 ± 0.4	81.5 ± 3.2	100 ± 0.0	100 ± 0.0	81.5 ± 3.2
	MagLap	0.0035 ± 0.0018	0.0036 ± 0.0018	0.0670 ± 0.0032	0.0045 ± 0.0008	0.0033 ± 0.0013	1.9 ± 0.4	66.5 ± 4.1	100 ± 0.0	100 ± 0.0	66.5 ± 4.1
	MagLap (Q = 5)	0.0039 ± 0.0021	0.0038 ± 0.0018	0.0504 ± 0.0011	0.0047 ± 0.0006	0.0065 ± 0.0018	2.4 ± 0.4	92 ± 1.9	100 ± 0.0	100 ± 0.0	92 ± 1.9
	MagLap (Q = 10)	0.0037 ± 0.0019	0.0038 ± 0.0018	0.0450 ± 0.0037	0.0038 ± 0.0006	0.0021 ± 0.0009	1.5 ± 0.4	95.5 ± 3.7	100 ± 0.0	100 ± 0.0	95.5 ± 3.7
ER	No PE	0.0039 ± 0.0022	0.0038 ± 0.0023	0.0486 ± 0.0039	0.0039 ± 0.0009	0.0030 ± 0.0019	2.8 ± 1.4	100 ± 0.0	100 ± 0.0	100 ± 0.0	100 ± 0.0
	Lap	0.0022 ± 0.0014	0.0021 ± 0.0014	0.0479 ± 0.0058	0.0037 ± 0.0013	0.0017 ± 0.0010	1.8 ± 0.9	99.5 ± 1.0	100 ± 0.0	100 ± 0.0	99.5 ± 1.0
	RRWP	0.0021 ± 0.0013	0.0021 ± 0.0013	0.0505 ± 0.0037	0.0033 ± 0.0013	0.0018 ± 0.0010	1.8 ± 0.8	99.5 ± 1.0	100 ± 0.0	100 ± 0.0	99.5 ± 1.0
	MagLap	0.0021 ± 0.0013	0.0021 ± 0.0013	0.0515 ± 0.0055	0.0029 ± 0.0004	0.0019 ± 0.0011	1.8 ± 0.8	99 ± 1.2	100 ± 0.0	100 ± 0.0	99 ± 1.2
	MagLap (Q = 5)	0.0022 ± 0.0014	0.0021 ± 0.0014	0.0456 ± 0.0068	0.0029 ± 0.0006	0.0017 ± 0.0010	1.8 ± 0.9	100 ± 0.0	100 ± 0.0	100 ± 0.0	100 ± 0.0
	Price	No PE	0.0149 ± 0.0020	0.0011 ± 0.0002	0.0524 ± 0.0030	0.0041 ± 0.0004	0.0017 ± 0.0000	2.9 ± 0.1	92.5 ± 1.6	100 ± 0.0	100 ± 0.0
Lap		0.0219 ± 0.0030	0.0010 ± 0.0002	0.0725 ± 0.0016	0.0476 ± 0.0034	0.0124 ± 0.0020	16.2 ± 2.0	99 ± 1.2	100 ± 0.0	100 ± 0.0	99 ± 1.2
RRWP		0.0231 ± 0.0034	0.0010 ± 0.0002	0.0837 ± 0.0022	0.0619 ± 0.0048	0.0123 ± 0.0027	17.0 ± 2.8	99 ± 1.2	100 ± 0.0	100 ± 0.0	99 ± 1.2
MagLap		0.0232 ± 0.0013	0.0012 ± 0.0001	0.0752 ± 0.0028	0.0531 ± 0.0059	0.0126 ± 0.0019	16.8 ± 2.1	97.5 ± 2.2	100 ± 0.0	100 ± 0.0	97.5 ± 2.2
MagLap (Q = 5)		0.0191 ± 0.0031	0.0010 ± 0.0001	0.0653 ± 0.0118	0.0239 ± 0.0023	0.0044 ± 0.0016	6.8 ± 1.7	99.5 ± 1.0	100 ± 0.0	100 ± 0.0	99.5 ± 1.0

We observe that that ER and Price graphs, due to their simplicity and highly regular generative processes, pose a relatively easy modeling challenge. As a result, performance is consistently high across all variants, including the baseline with no positional encoding. In contrast, the SBM and ER-DAG datasets present more intricate structural patterns, which amplify the benefits of informed positional encodings. In these cases, clear performance gaps emerge between the baseline, non-directed encodings (e.g., Lap), and directed-aware methods such as RRWP and MagLapPE.

These differences highlight the importance of encoding directionality to faithfully capture the distribution of more structurally diverse directed graphs. For this reason, in the main paper we focus our synthetic evaluations on SBM and ER-DAG, where the modeling challenge is sufficiently rich to reveal the comparative strengths of different modeling strategies.

### H.3 ER vs DAG performance

To evaluate the structural quality of generated synthetic directed acyclic graphs, we defined a composite validity metric that captures two key properties: (i) the percentage of generated graphs that are Directed Acyclic Graphs (DAGs), and (ii) the percentage that follow the target structural distribution (e.g. Erdős-Renyi). The validity score is computed as the proportion of generated graphs that satisfy both criteria. For completeness, we also report each component individually to disentangle the contributions of acyclicity and distributional alignment.

Table 13: ER vs DAG accuracy

Model	% DAG	% ER	Valid
Training set	100	99.2	99.2
MLE	0 ± 0.0	97 ± 2.1	0 ± 0.0
D-VAE	100 ± 0.0	0 ± 0.0	0 ± 0.0
LAYERDAG	100 ± 0.0	21.5 ± 2.7	21.5 ± 2.7
DIGRESS	35 ± 4.2	98.5 ± 2.0	34 ± 4.1
DEFOG	21.5 ± 2.7	100 ± 0.0	21.5 ± 2.7
DIRECTO-DD RRWP	79 ± 3.7	100 ± 0.0	79 ± 3.7
DIRECTO-DD MagLap ( $Q = 10$ )	86 ± 9.4	99 ± 1.2	85 ± 10.2
DIRECTO RRWP	94 ± 1.0	100 ± 0.0	94 ± 1.0
DIRECTO MagLap ( $Q = 10$ )	99.5 ± 1.0	92.5 ± 2.7	92 ± 3.7

As shown in Table 13, baselines such as MLE and LAYERDAG exhibit a stark imbalance: while LAYERDAG guarantees acyclicity, both fail to model the target ER distribution, resulting in low overall validity. On the other hand, MLE closely aligns with the distribution but fails to generate acyclic graphs.

In contrast, diffusion- and flow matching-based methods paired with dual attention and relevant directed positional encodings achieve strong performance on both fronts, demonstrating their ability to generate structurally valid DAGs that also align with the underlying data distribution. This highlights the limitations of purely autoregressive or heuristic DAG-specific approaches when used in isolation.

### H.4 Effect of dataset size

To evaluate the effect on the number of graphs available at training time, we conduct an ablation study using the synthetic ER-DAG dataset in two configurations: the standard size and a variant with 10× more training, test, and validation samples. This setup allows us to assess whether the method encodings benefit from increased data. We compare the different positional encodings for discrete diffusion using dual attention, with results in Table 14. Overall, we see that increasing the

Table 14: Effect of the dataset size (using DIRECTO-DD).

Dataset	Model	Out-degree ↓	In-degree ↓	Clustering ↓	Spectre ↓	Wavelet ↓	Ratio ↓	Valid ↑	Unique ↑	Novel ↑	V.U.N. ↑
Standard	Train set	0.0113	0.0103	0.0355	0.0038	0.0024	1.0	99.2	100	0	0
	Lap	0.0138 ± 0.0038	0.0144 ± 0.0042	0.0462 ± 0.0071	0.0055 ± 0.0011	0.0052 ± 0.0015	1.5 ± 0.3	67 ± 5.3	100 ± 0.0	100 ± 0.0	67 ± 5.3
	RRWP	0.0142 ± 0.0040	0.0129 ± 0.0034	0.0408 ± 0.0053	0.0055 ± 0.0010	0.0048 ± 0.0014	1.4 ± 0.3	79 ± 3.7	100 ± 0.0	100 ± 0.0	79 ± 3.7
	MagLap	0.0142 ± 0.0044	0.0135 ± 0.0034	0.0438 ± 0.0071	0.0057 ± 0.0013	0.0046 ± 0.0010	1.4 ± 0.3	69 ± 6.4	100 ± 0.0	100 ± 0.0	69 ± 6.4
	MagLap ( $Q = 5$ )	0.0135 ± 0.0032	0.0140 ± 0.0045	0.0596 ± 0.0081	0.0061 ± 0.0007	0.0037 ± 0.0017	1.4 ± 0.2	78.5 ± 2.5	100 ± 0.0	100 ± 0.0	78.5 ± 2.5
x 10	Train set	0.0002	0.0003	0.0021	0.0004	0.0000	1.0	99.9	100	0	0
	Lap	0.00035 ± 0.0007	0.0032 ± 0.0008	0.0261 ± 0.0025	0.0024 ± 0.0003	0.0006 ± 0.0001	10.5 ± 1.3	85.5 ± 2.4	100 ± 0.0	100 ± 0.0	85.5 ± 2.4
	RRWP	0.0030 ± 0.0008	0.0031 ± 0.0006	0.0277 ± 0.0075	0.0024 ± 0.0004	0.0006 ± 0.0002	10.1 ± 2.2	94 ± 4.4	100 ± 0.0	100 ± 0.0	94 ± 4.4
	MagLap	0.0030 ± 0.0006	0.0033 ± 0.0005	0.0305 ± 0.0051	0.0025 ± 0.0005	0.0007 ± 0.0003	14.5 ± 2.4	89.5 ± 3.7	100 ± 0.0	100 ± 0.0	89.5 ± 3.7
	MagLap ( $Q = 5$ )	0.0031 ± 0.0008	0.0028 ± 0.0006	0.0237 ± 0.0028	0.0022 ± 0.0006	0.0008 ± 0.0001	9.6 ± 1.6	93.5 ± 2.5	100 ± 0.0	100 ± 0.0	93.5 ± 2.5

dataset size significantly improves generation performance across all positional encoding variants,

confirming that additional training data helps models better capture structural patterns. However, this performance gain comes at the cost of substantially longer training times and greater computational demand ( $\sim 12\text{h}$  for the standard dataset vs  $\sim 32\text{h}$  for the bigger version). These trade-offs motivate our focus on architectural innovations such as employing discrete flow matching as more efficient alternatives to scaling purely through data and compute.

### H.5 Impact of sampling optimization using discrete flow matching

To better understand the influence of the three sampling hyperparameters discussed in Appendix C: time distortion, stochasticity coefficient ( $\eta$ ), and target guidance factor ( $\omega$ ) on generative performance, we analyze their effect on the V.U.N. and the structural ratio. Specifically, we present performance curves for the four primary datasets reported in the main results table: SBM, RRWP, TPU Tiles, and Visual Genome. For each dataset, we evaluate the impact of these parameters under two positional encoding strategies: RRWP and MagLap. We report the results for 100 sampling steps and 5 different sampling runs (except for TPU Tiles where only 1 run was performed due to computational constraints).

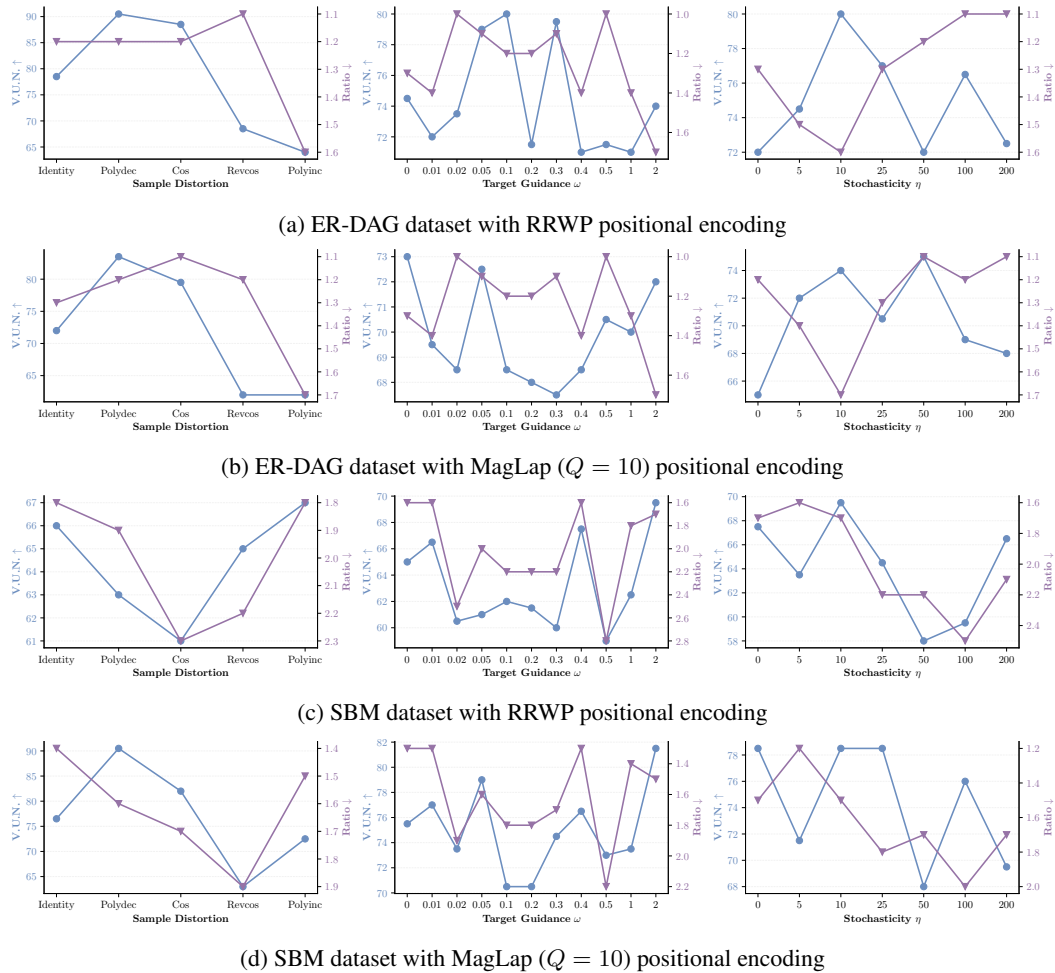
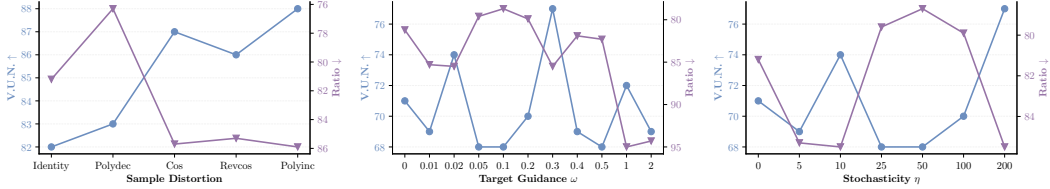


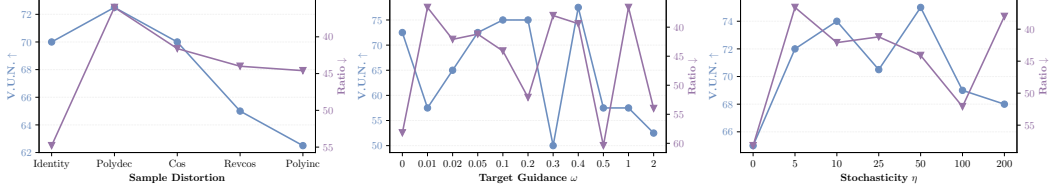
Figure 4: Sampling optimization curves for the synthetic datasets with 100 sampling steps and 5 sampling runs. We represent V.U.N. (blue) and MMD ratio (purple) and optimize for best trade-off for each of the three parameters individually.

The results for the synthetic datasets in Figure 4 illustrate that the sampling hyperparameters meaningfully influence the generative performance. We observe that different values can lead to notable variations in both V.U.N. and the structural ratio. However, a higher V.U.N. does not necessarily correspond to a lower ratio. While certain configurations tend to perform well across both RRWP

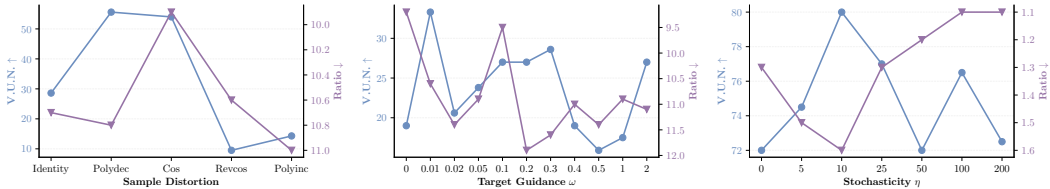
and MagLap positional encodings, the improvements are generally modest, suggesting that optimal settings may vary slightly depending on the dataset and positional encoding strategy used.



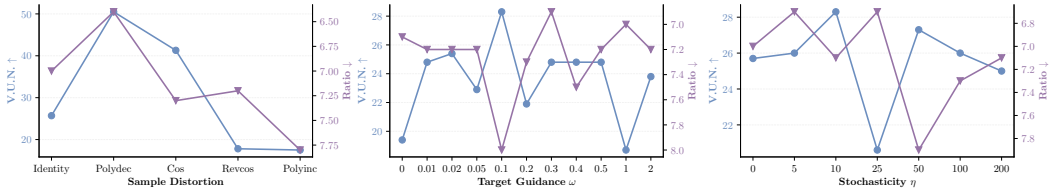
(a) TPU Tiles dataset with RRWP positional encoding



(b) TPU Tiles dataset with MagLap ( $Q = 10$ ) positional encoding



(c) Visual Genome dataset with RRWP positional encoding



(d) Visual Genome dataset with MagLap ( $Q = 10$ ) positional encoding

Figure 5: Sampling optimization curves for the synthetic datasets with 100 sampling steps and 5 sampling runs. We represent V.U.N. (blue) and MMD ratio (purple) and optimize for best trade-off for each of the three parameters individually.

A similar pattern is observed in the results for the real-world datasets (TPU Tiles and Visual Genome), as shown in Figure 5. The sampling hyperparameters continue to affect generation performance, and there is no clear one-to-one relationship between V.U.N. and ratio. As with the synthetic datasets, some hyperparameter combinations show slightly more consistent behavior across positional encodings, but overall, the best hyperparameters combination remain dependent on the dataset and positional encoding used.

## I Iterative Refinement Methods for Graph Generation

### I.1 Graph iterative refinement methods

Within the realm of undirected graph generation, discrete state-space iterative refinement approaches [67, 74, 60, 55] have emerged as a powerful framework for capturing the intricate dependencies that govern target graph distributions. These methods achieve state-of-the-art performance by naturally aligning with the structure of graphs: they operate directly in discrete state spaces, matching the inherent discreteness of adjacency matrices, and respect node permutation equivariances due to their one-shot prediction formulation. These characteristics make iterative refinement approaches particularly well-suited for the task of directed graph generation.

These methods comprise two main processes: a noising process and a denoising process. For consistency, we define  $t = 0$  as corresponding to fully noised graphs and  $t = 1$  to clean graphs. The noising process runs from  $t = 1$  to  $t = 0$ , progressively corrupting the original graphs, while the denoising process learns how to reverse this trajectory, running from  $t = 0$  to  $t = 1$ .

Denoising is performed using a neural network parametrized by  $\theta$ ,

$$\mathbf{p}_{1|t}^\theta(\cdot|G_t) = \left( \left( p_{1|t}^{\theta,(n)}(x_1^{(n)} | G_t) \right)_{1 \leq n \leq N}, \left( p_{1|t}^{\theta,(i,j)}(e_1^{(i,j)} | G_t) \right)_{1 \leq i \neq j \leq N} \right), \quad (41)$$

which predicts categorical distributions over nodes and edges given a noised graph  $G_t$ . In practice,  $\mathbf{p}_{1|t}^\theta(\cdot|G_t)$  is parameterized using a graph transformer such as [16], which allows for expressive modeling of complex graph structures. The network is trained using a cross-entropy loss applied independently to each node and each edge:

$$\mathcal{L} = \mathbb{E}_{t, G_1, G_t} \left[ - \sum_n \log \left( p_{1|t}^{\theta,(n)}(x_1^{(n)} | G_t) \right) - \lambda \sum_{i \neq j} \log \left( p_{1|t}^{\theta,(i,j)}(e_1^{(i,j)} | G_t) \right) \right], \quad (42)$$

where the expectation is taken over time  $t$  sampled from a predefined distribution over  $[0, 1]$  (e.g., uniform);  $G_1 \sim p_1(G_1)$  is a clean graph from the dataset; and  $G_t \sim p_t(G_t|G_1)$  is its noised version at time  $t$ . The hyperparameter  $\lambda \in \mathbb{R}^+$  controls the relative weighting between node and edge reconstruction losses. Once the denoising network is trained, different graph iterative refinement methods vary in how they leverage the predicted  $\mathbf{p}_{1|t}^\theta(\cdot|G_t)$  to progressively recover the clean graphs.

## I.2 Discrete flow matching for graph generation

Among graph iterative refinement methods, Discrete Flow Matching (DFM) [9, 20] has recently emerged as a particularly powerful framework. By decoupling the training and sampling processes, DFM enables a broader and more flexible design space, which has been shown to improve generative performance. This framework has proven particularly effective for undirected graph generation [55].

The noising process in DFM is defined as a linear interpolation between the data distribution and a pre-specified noise distribution. This interpolation is applied independently to each variable, corresponding to each node and each edge in the case of graphs:

$$p_{t|1}^X(x_t^{(n)} | x_1^{(n)}) = t \delta(x_t^{(n)}, x_1^{(n)}) + (1 - t) p_{\text{noise}}^X(x_t^{(n)}), \quad (43)$$

where  $\delta(\cdot, \cdot)$  is the Kronecker delta and  $p_{\text{noise}}^X$  is a reference distribution over node categories. A similar construction is used for edges. Therefore, the complete noising process corresponds to independently noising each node and edge through  $p_{t|1}^X$  and  $p_{t|1}^E$ , respectively.

To reverse this process, DFM models denoising as a Continuous-Time Markov Chain (CTMC). Starting from an initial distribution  $\mathbf{p}_0$ , the generative process evolves according to:

$$\mathbf{p}_{t+\Delta t|t}(G_{t+\Delta t} | G_t) = \delta(G_t, G_{t+\Delta t}) + \mathbf{R}_t(G_t, G_{t+\Delta t}) dt, \quad (44)$$

where  $\mathbf{R}_t$  is the CTMC rate matrix. In practice, this update is approximated over a finite interval  $\Delta t$ , in an Euler method step, with the rate matrix estimated from the network predictions  $\mathbf{p}_{1|t}^\theta(\cdot | G_t)$  via:

$$\mathbf{R}_t^\theta(G_t, G_{t+\Delta t}) = \sum_n \delta(G_t^{\setminus(n)}, G_{t+\Delta t}^{\setminus(n)}) \mathbb{E}_{p_{1|t}^{\theta,(n)}(x_1^{(n)} | G_t)} \left[ R_t^{(n)}(x_t^{(n)}, x_{t+\Delta t}^{(n)} | x_1^{(n)}) \right] \quad (45)$$

$$+ \sum_{i \neq j} \delta(G_t^{\setminus(i,j)}, G_{t+\Delta t}^{\setminus(i,j)}) \mathbb{E}_{p_{1|t}^{\theta,(i,j)}(e_1^{(i,j)} | G_t)} \left[ R_t^{(i,j)}(e_t^{(i,j)}, e_{t+\Delta t}^{(i,j)} | e_1^{(i,j)}) \right], \quad (46)$$

where the  $G^{\setminus(d)}$  denote the full graph  $G$  except variable  $d$  (node or edge). The Kronecker deltas ensure that each variable-specific rate matrix,  $R_t^{(n)}$  or  $R_t^{(i,j)}$ , is applied independently at each node and edge, respectively. Finally, each node-specific rate matrix is defined as:

$$R_t(x_t^{(n)}, x_{t+\Delta t}^{(n)} | x_1^{(n)}) = \frac{\text{ReLU} \left[ \partial_t p_{t|1}(x_{t+\Delta t}^{(n)} | x_1^{(n)}) - \partial_t p_{t|1}(x_t^{(n)} | x_1^{(n)}) \right]}{X_t^{>0} p_{t|1}(x_t^{(n)} | x_1^{(n)})}, \quad (47)$$

for each node  $x^{(n)}$ , where  $X_t^{>0} = \left| \left\{ x_t^{(n)} : p_{t|1}(x_t^{(n)} | x_1^{(n)}) > 0 \right\} \right|$ . An analogous definition applies for edge rate matrices.

### I.3 Discrete diffusion for graph generation

Among discrete diffusion-based models for undirected graphs, DIGRESS [67], grounded in the structured discrete diffusion framework [3], has been particularly influential. This approach mostly differs from the DFM-based formulation described in Appendix I.2, as it operates in discrete time, with the denoising process modeled as a Discrete-Time Markov Chain (DTMC), in contrast to the continuous-time formulation used in DFM.

The forward, or noising, process is modeled as a Markov noise process  $q$ , which generates a sequence of progressively noised graphs  $G_t$ , for  $t = 1, \dots, T$ . At each timestep, node and edge tensors are perturbed using categorical transition matrices  $[\mathbf{Q}_t^X]^{(i,j)} = q(x_t = j \mid x_{t-1} = i)$  and  $[\mathbf{Q}_t^E]^{(i,j)} = q(e_t = j \mid e_{t-1} = i)$ , respectively. This process induces structural changes such as edge addition or deletion, and edits to node and edge categories. The transition probabilities can be summarized as:

$$q(G_t \mid G_{t-1}) = (\mathbf{X}_{t-1} \mathbf{Q}_t^X, \mathbf{E}_{t-1} \mathbf{Q}_t^E) \quad \text{and} \quad q(G_t \mid G) = \left( \mathbf{X} \prod_{i=1}^t \mathbf{Q}_i^X, \mathbf{E} \prod_{i=1}^t \mathbf{Q}_i^E \right). \quad (48)$$

In practice, these noise matrices are implemented based on the *marginal* noise model, defined as:

$$\mathbf{Q}_t^X = \alpha^t \mathbf{I} + (1 - \alpha^t) \mathbf{1}_X \mathbf{m}_X^\top \quad \text{and} \quad \mathbf{Q}_t^E = \alpha^t \mathbf{I} + (1 - \alpha^t) \mathbf{1}_E \mathbf{m}_E^\top,$$

where  $\alpha^t$  transitions from 1 to 0 with  $t$  according to the popular cosine scheduling [49]. The vectors  $\mathbf{1}_X \in \{1\}^X$  and  $\mathbf{1}_E \in \{1\}^{E+1}$  are filled with ones, and  $\mathbf{m}_X \in \Delta^X$  and  $\mathbf{m}_E \in \Delta^{E+1}$  are vectors filled with the marginal node and edge distributions, respectively<sup>3</sup>.

This noising process can be rewritten using the analogous notation to the one used for DFM in Eq. (49) as:

$$p_{t'|1}^X(x_{t'}^{(n)} \mid x_1^{(n)}) = \bar{\alpha}(t') \delta(x_{t'}^{(n)}, x_1^{(n)}) + (1 - \bar{\alpha}(t')) p_{\text{noise}}^X(x_{t'}^{(n)}), \quad (49)$$

with  $t' = 1 - \frac{t}{T}$  and  $\bar{\alpha}(t') = \cos\left(\frac{\pi}{2} \frac{1-t'+s}{1+s}\right)^2$ , with a small  $s$ . Importantly, this function is only evaluated in the discrete values of time considered for the DTMC associated to the diffusion model. For the remaining of this section, we consider the transformed variable  $t'$  as the reference time variable.

In the reverse, or denoising, process, a clean graph is progressively built leveraging the denoising neural network predictions  $p_{1|t'}^\theta(\cdot \mid G_t')$ , analogously to the DFM setting. In particular, the model begins from a noise sample  $G_0$  and iteratively predicts the clean graph  $G_1$  by modeling node and edge distributions conditioned on the full graph structure. The reverse transition is defined as:

$$p_{t'+\Delta t'|t'}^\theta(G_{t'+\Delta t'} \mid G_{t'}) = \prod_{i=1}^N p_{t'+\Delta t'|t'}^\theta(x_{t'+\Delta t'}^{(n)} \mid G_{t'}) \prod_{1 \leq i < j \leq N} p_{t'+\Delta t'|t'}^\theta(e_{t'+\Delta t'}^{(i,j)} \mid G_{t'}). \quad (50)$$

with each of the node and edge denoising terms are computed through the following marginalization:

$$p_{t'+\Delta t'|t'}^\theta(x_{t'+\Delta t'}^{(n)} \mid G_{t'}) = \sum_{x_1^{(n)} \in \{1, \dots, X\}} p_{t'+\Delta t'|1, t'}^\theta(x_{t'+\Delta t'}^{(n)} \mid x_1^{(n)}, G_{t'}) p_{1|t'}^{\theta, (n)}(x_1^{(n)} \mid G_{t'}), \quad (51)$$

and similarly for edges. To compute the missing posterior term in Eq. (51),  $p_{t'+\Delta t'|1, t'}^\theta(x_{t'+\Delta t'}^{(n)} \mid x_1^{(n)}, G_{t'})$ , we equate it to the posterior term of the forward process:

$$p_{t'+\Delta t'|1, t'}^\theta(x_{t'+\Delta t'}^{(n)} \mid x_1^{(n)}, G_{t'}) = \begin{cases} \frac{\mathbf{x}_{t'}^{(n)} (\mathbf{Q}_{t'}^X)^\top \odot \mathbf{x}_1^{(n)} \mathbf{Q}_{t'+\Delta t'}^X}{\mathbf{x}_{t'}^{(n)} \mathbf{Q}_{t'}^X \mathbf{x}_1^{(n)}} & \text{if } q(x_{t'}^{(n)} \mid x_1^{(n)}) > 0, \\ 0 & \text{otherwise,} \end{cases} \quad (52)$$

where  $\mathbf{x}_{t'}^{(n)}$  and  $\mathbf{x}_1^{(n)}$  denote the vectorized versions of  $x_{t'}^{(n)}$  and  $x_1^{(n)}$ , respectively. Crucially, and contrarily to DFM, the sampling strategy with discrete diffusion is fixed at training time, which restricts the design space of this generative framework.

<sup>3</sup>We denote the probability simplex of the state-space of cardinality  $Z$  by  $\Delta^Z$

## J Visualizations

In this section, we present visualizations of the digraphs generated with DIRECTO for the different synthetic and real-world datasets and combinations of positional encodings reported in the main paper. To allow for a fair comparison between original and generated digraphs, we additionally report digraphs from the train splits of the original datasets.

Original digraphs for the SBM dataset are shown in Figure 6. Figure 7 and Figure 8 show examples of digraphs from the Stochastic Block Model (SBM), where clear community structures are visible, consistent with the underlying block partitioning. These visualizations help illustrate how the positional encodings preserve modularity and inter-cluster connectivity. Similarly, Figure 9 shows original digraphs from the ER-DAG dataset, with Figure 10 and Figure 11 displaying generated digraphs from the Erdős–Rényi (ER-DAG) model. In this case, digraphs are plotted with nodes in topological order, to highlight the acyclicity.

For the real-world datasets, in particular for the TPU Tiles dataset, which consists of directed acyclic graphs (DAGs) representing hardware execution plans, we can see the original DAGs in Figure 12. From the visualizations in Figure 13 and Figure 14 we see that the model is able to capture and generalize across structural patterns that emerge in computational workloads. In a similar way as before, digraphs are represented with nodes in topological order to highlight acyclicity.

Finally, for the Visual Genome dataset, we represent the three different node types: objects (blue), relationships (red) and attributes (green), alongside their respective node label. Figure 15 shows the original graphs, while Figure 16 and Figure 17 report the generations. They show how the model effectively captures the semantic and relational structure across these node categories, learning meaningful patterns that align with human understanding (i.e. *a person wears a yellow shirt*, or *a white cloud in the sky*).

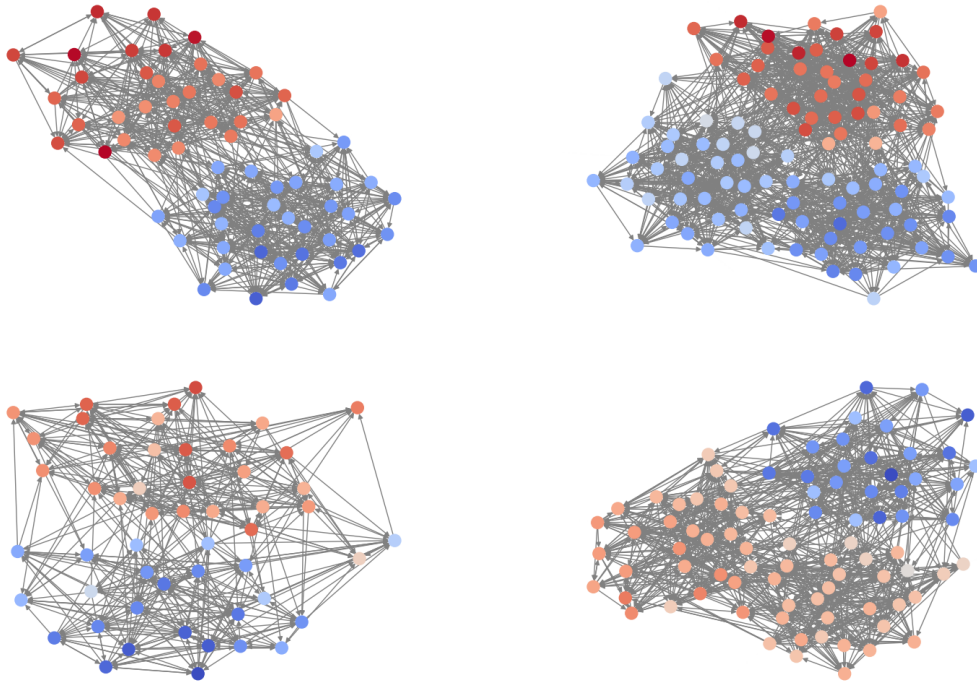


Figure 6: Visualizations of original synthetic digraphs from the train splits of the SBM dataset.

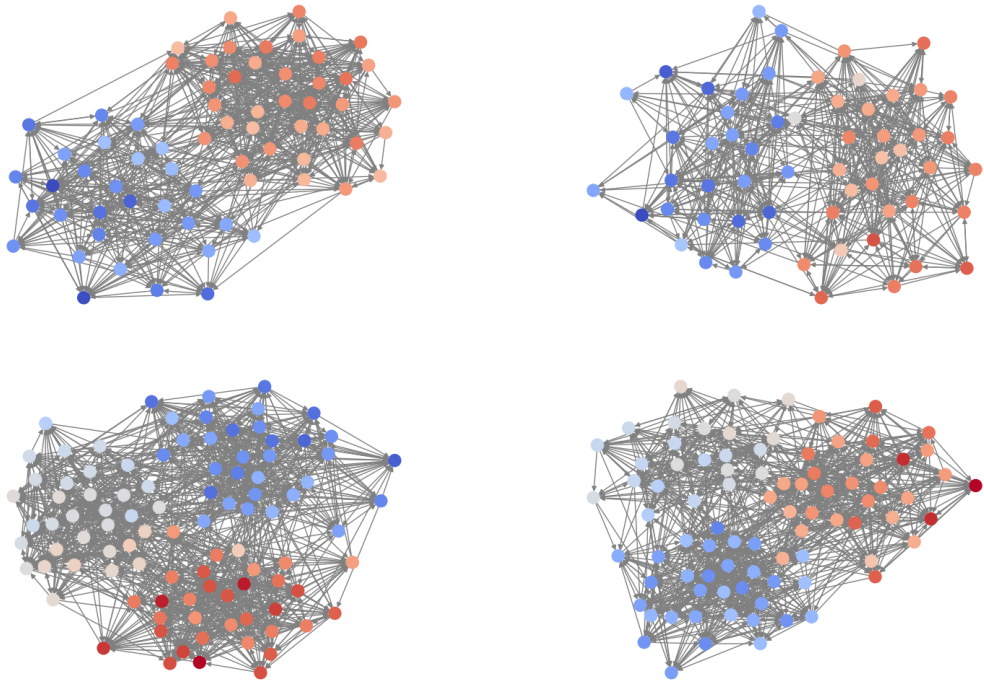


Figure 7: Visualizations of four generated digraphs for the SBM dataset with RRWP positional encoding.

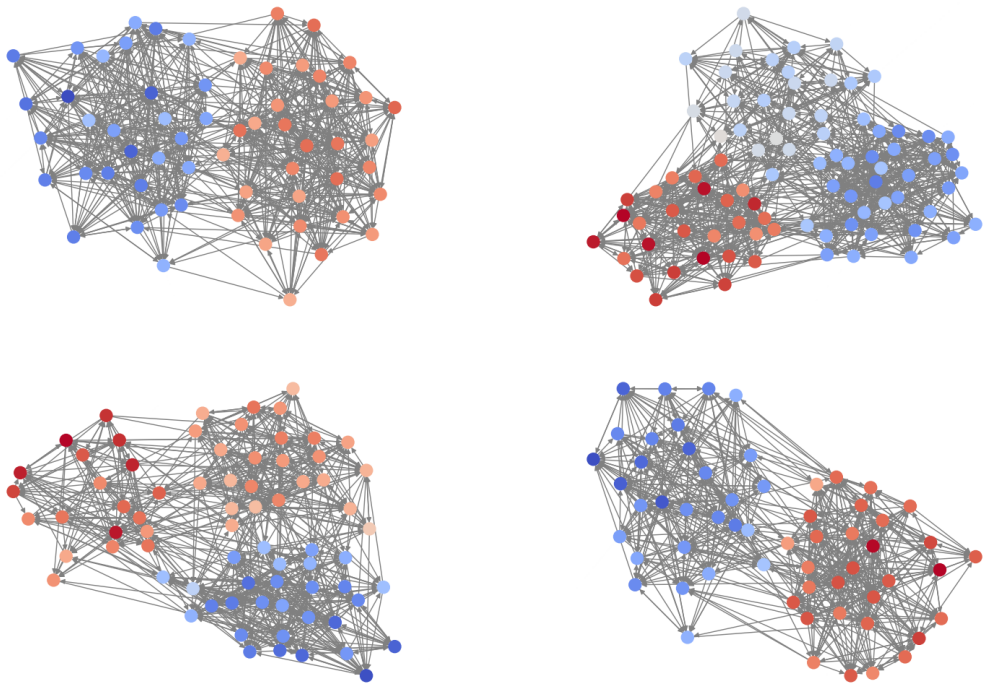


Figure 8: Visualizations of four generated digraphs for the SBM dataset with MagLap ( $Q = 10$ ) positional encoding.

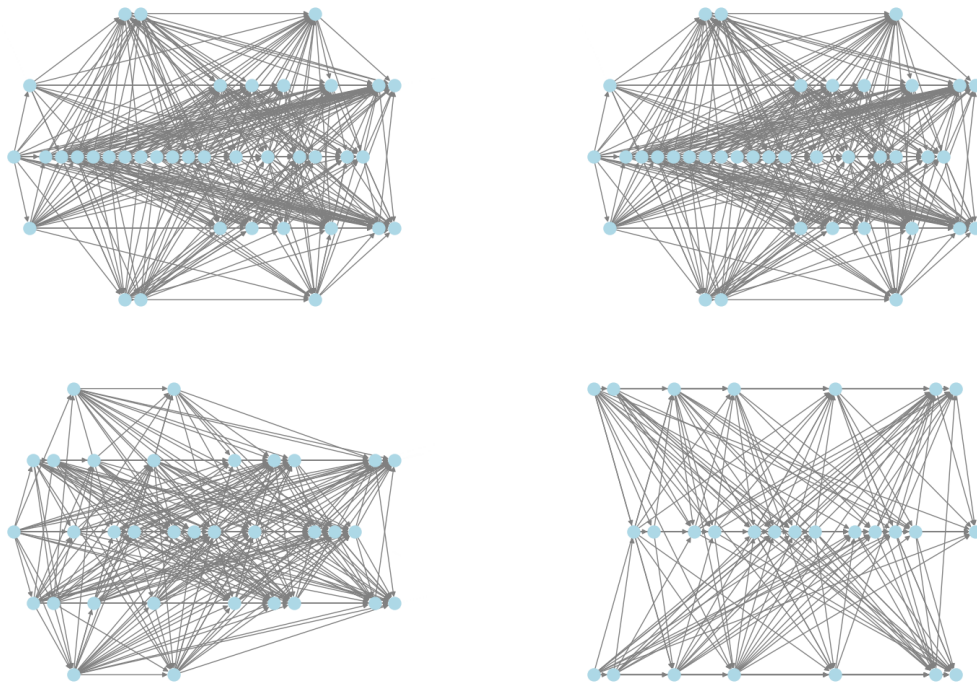


Figure 9: Visualizations of original synthetic digraphs from the train splits of the ER-DAG datasets. Nodes are in topological ordering to highlight the acyclic structure.

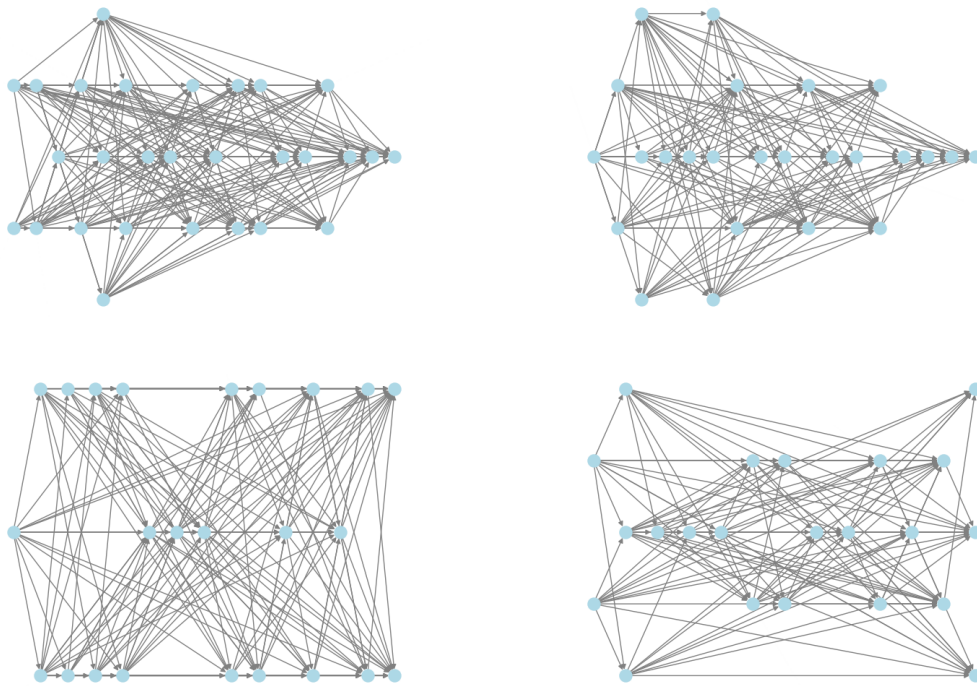


Figure 10: Visualizations of four generated digraphs for the ER-DAG dataset with RRWP positional encoding. Nodes are in topological ordering to highlight the acyclic structure.

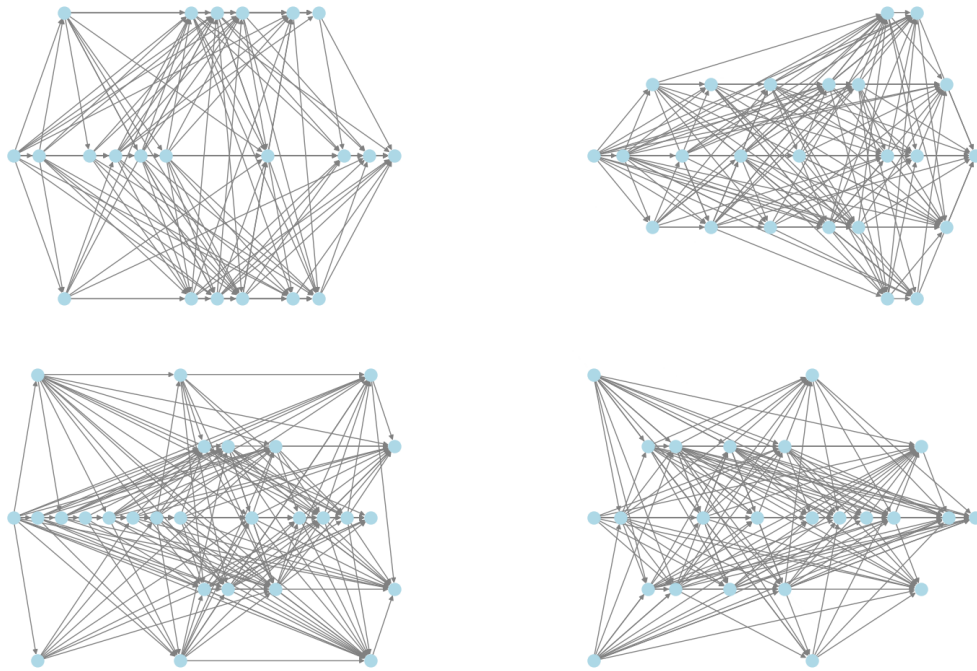


Figure 11: Visualizations of four generated digraphs for the ER-DAG dataset with MagLap ( $Q = 10$ ) positional encoding. Nodes are in topological ordering to highlight the acyclic structure.

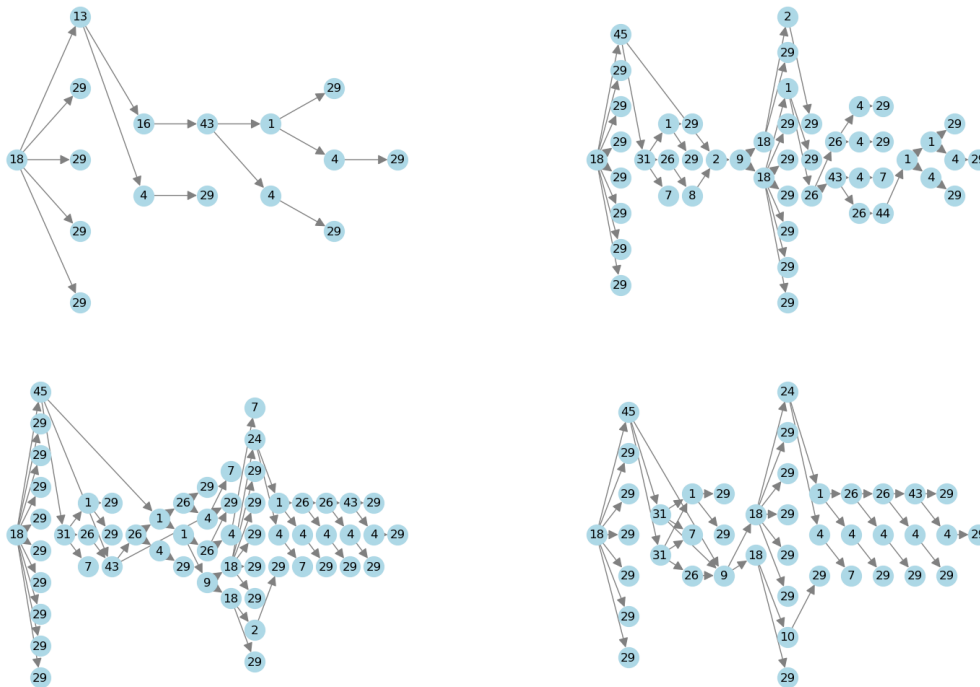


Figure 12: Visualizations of original real-world digraphs from the train splits of the TPU Tiles dataset. Nodes are in topological ordering to highlight the acyclic structure.

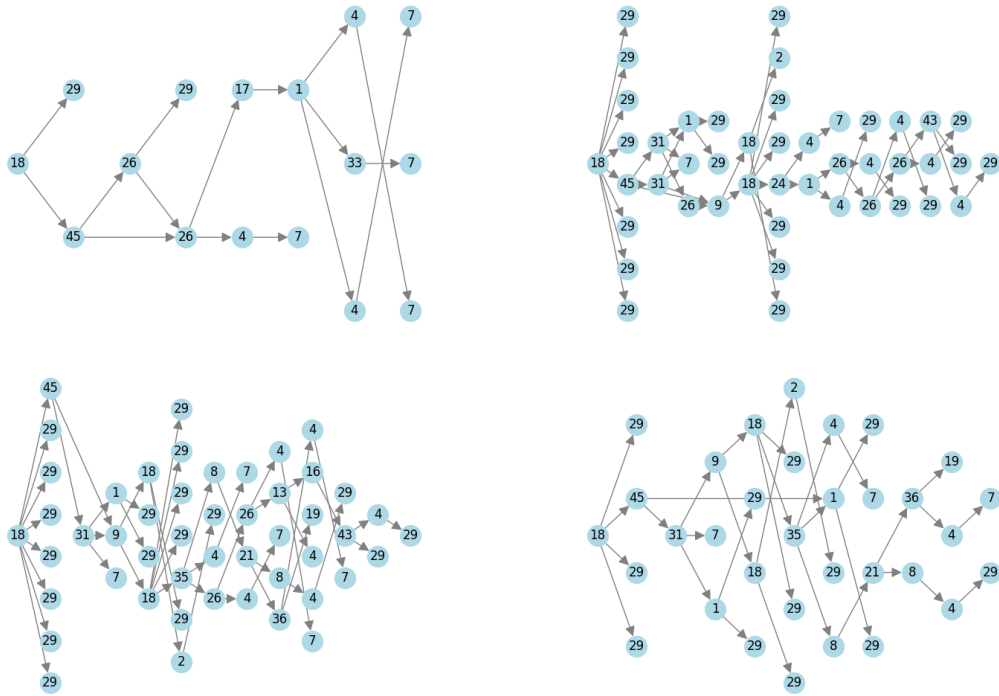


Figure 13: Visualizations of four generated dgraphs for the TPU Tiles dataset with RRWP positional encoding. Nodes are in topological ordering to highlight the acyclic structure.

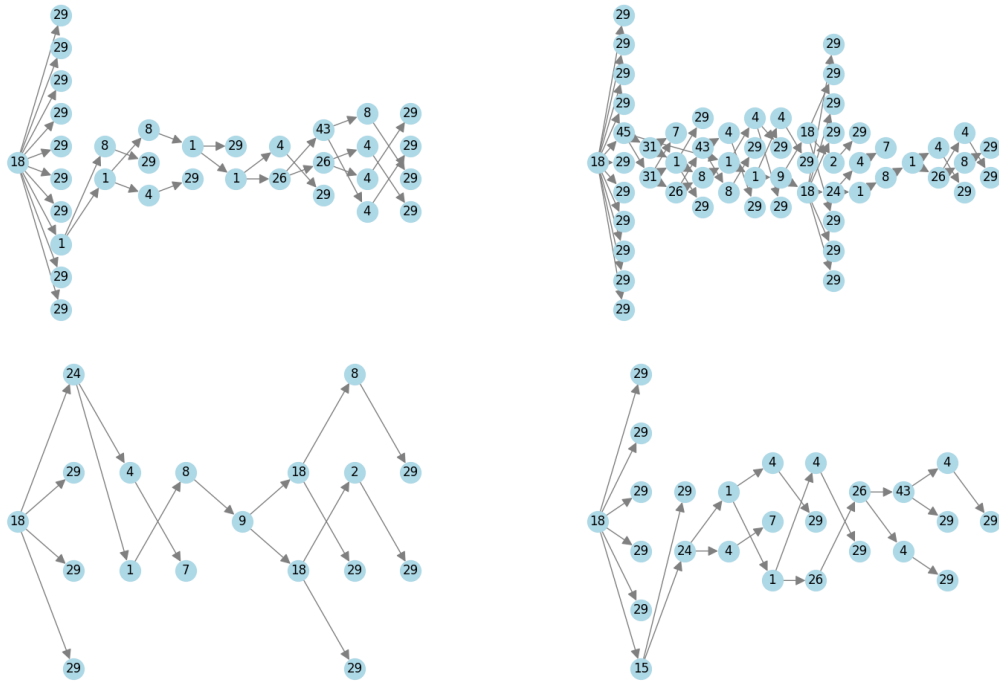


Figure 14: Visualizations of four generated digraphs for the TPU Tiles dataset with MagLap ( $Q = 5$ ) positional encoding. Nodes are in topological ordering to highlight the acyclic structure.

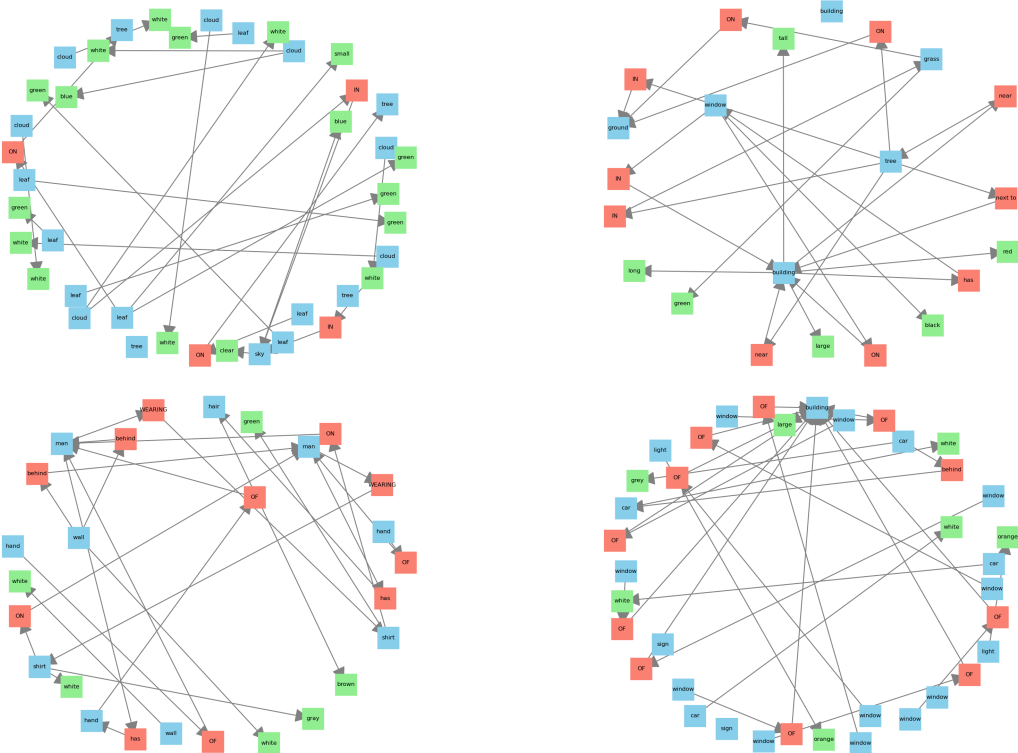


Figure 15: Visualizations of original real-world digraphs from the train splits of the Visual Genome dataset. Nodes represent objects (blue), relationships (red), and attributes (green).

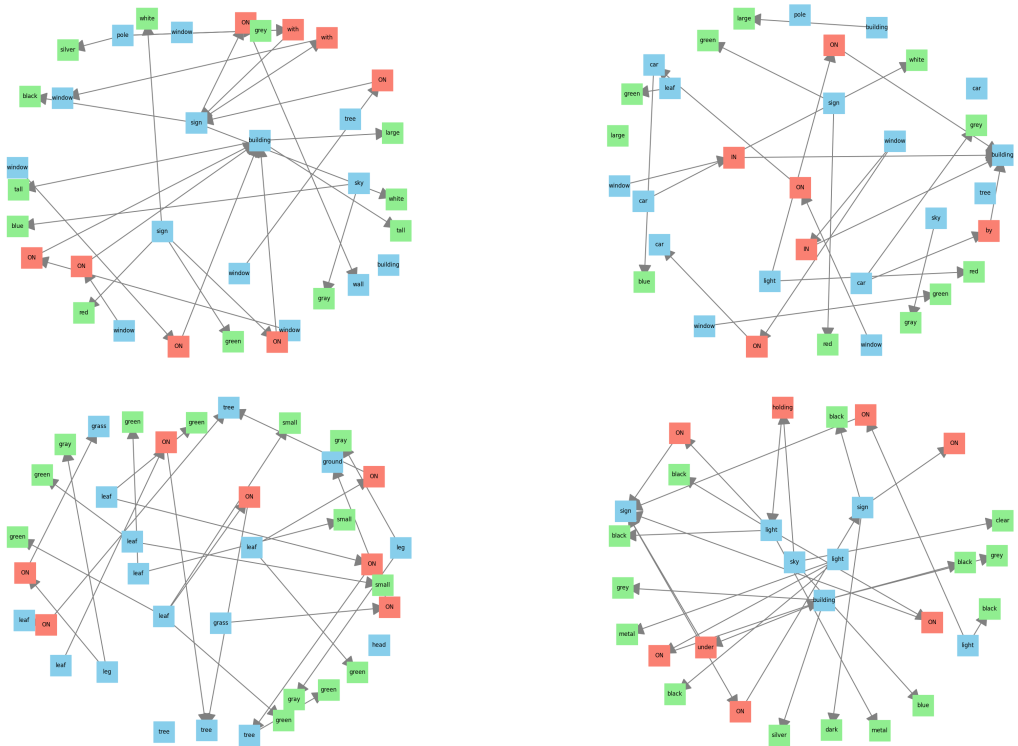


Figure 16: Visualizations of four generated digraphs for the Visual Genome dataset with RRWP positional encoding. Nodes represent objects (blue), relationships (red), and attributes (green).

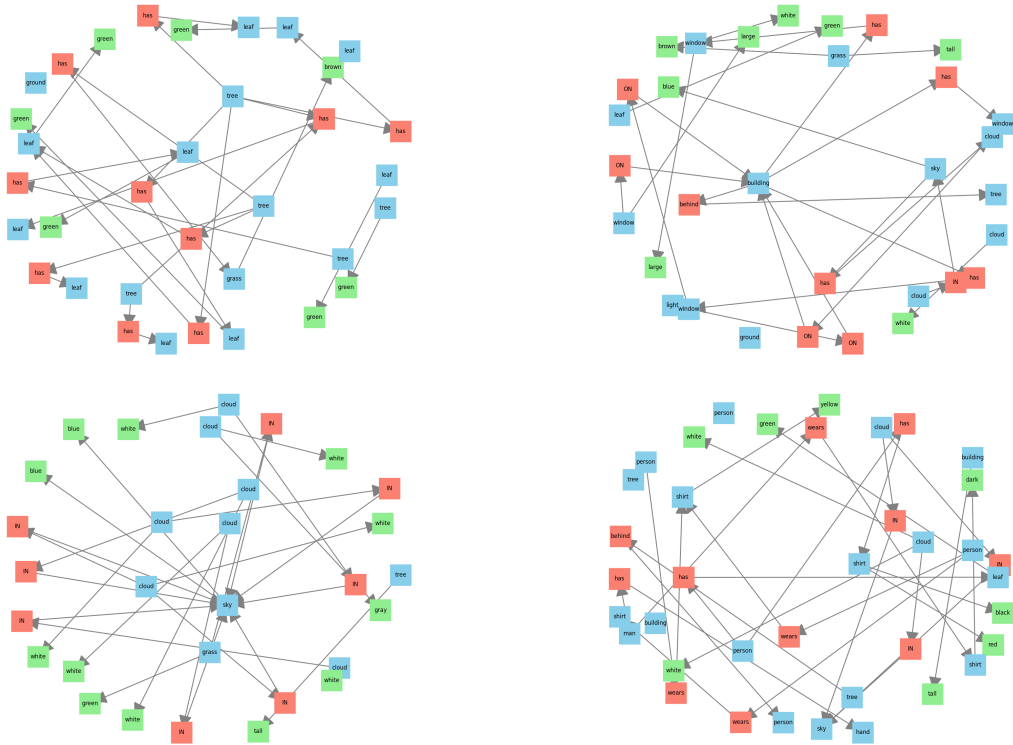


Figure 17: Visualizations of generated digraphs for the Visual Genome dataset with MagLap ( $Q = 5$ ) positional encoding. Nodes represent objects (blue), relationships (red), and attributes (green).

## K Impact statement and limitations

The objective of this work is to advance methodologies for the generation of directed graphs by introducing architectural mechanisms that explicitly model directionality and asymmetric relationships. Directed graphs are central to a wide range of applications, including causal inference, traffic modeling, and biological network analysis. Accordingly, improvements in directed graph generation have the potential to support progress in scientific research, decision-making systems, infrastructure design, or causal discovery.

The proposed framework enhances the expressiveness of generative models to directed graphs, and, at the moment, we do not identify any immediate societal risks associated with its deployment in its current form. Moreover, although the method is capable of generating structured and semantically meaningful graphs, the scale and complexity of these outputs remain limited, which may difficult direct applicability in high-impact domains such as real-time clinical diagnostics or large-scale policy modeling at this stage.